# ON CYLINDERS UNDERGOING ONE- AND TWO-DEGREE OF FREEDOM FORCED VIBRATIONS IN A STEADY FLOW

*Thesis by*
*David Jeon*

In Partial Fulfillment of the Requirements
for the Degree of
Doctor of Philosophy

California Institute of Technology
Pasadena, California

2000

(submitted May 19, 2000)

© 2000

David Jeon

All rights reserved.

# Acknowledgments

I would like to thank the Living God, whose words spoke into being a universe of endless complexity and humor. Studying the nature of His handiwork is a constant source of amazement and humility for me.

I would also like to thank my family for their constant and enduring support. My parents, Ike and Soon, were with me always, encouraging me and laying a firm foundation for me to grow on. My sister, Sarah, who has always looked out for me – and tirelessly proofread this thesis.

I must also thank my advisor, Dr. Morteza Gharib. I shudder to think of the work he does behind the scenes so that students like myself have such a wonderful opportunity to work here. He was a bottomless well of ideas and challenges – and was always able to find means to realize them.

Also I would like to thank Professors Roshko and Leonard for their insights into bluff body flows. Their wisdom and experience undergirds this work.

And those without whom my stay at GALCIT would not have been complete: Brad Dooley, for hours of discussions on all things football and the consumption of SPAM in its many glorious incarnations; Michael Ol, for countless discussions/arguments on cars and the principles of OLism; Ryan Mackey, for the never-ending search for the perfect barbeque; and Doug Shiels, for his ever delightfully quirky views on the world.

And the people who have contributed scientifically: Flavio Noca, for force deduction techniques and all things cylinder; Michael Ol and Rich Eastvedt, for building the water tunnel I used; Edmond Rambod, for the vortex ring experiments; Ron Henderson, for the stability analysis of the cylinder wake; and Jerry Shan, with whom the starting flow experiments were performed.

Special thanks to the Office of Naval Research for supporting the research that went into this thesis and Professor Raichlen for providing space for the water tunnel in Keck and insights that helped get the tunnel running.

# Abstract

Formation of vortices in the near wake of circular cylinders is discussed. Two different cases are compared: starting flow around an initially stationary cylinder and flow around an oscillating cylinder in a steady freestream. The effects of formation time on the morphology of the vortices are shown, as well as some consequences thereof.

For starting flows, the critical formation time defines the point where the wake transitions from the initially symmetrical state to the intermediate asymmetrical state. The asymmetrical state breaks down into the periodic shedding state normally associated with cylinder flows. It appears that the wake reaches a critical level of vorticity annihilation at the critical time. This triggers an exponential growth of asymmetry in the near wake. Evidence of this process can also be seen in the early time force data.

For oscillating flows, the critical time defines the transition from vortex to vortex-and-tail morphology. First, phase averaged vorticity fields are presented showing the changes in the wake with forcing frequency and streamwise motion. These changes are related to the formation time, and related to similar effects seen in other flows. In addition, prolonged formation is related to the observed switch in the phase of the vortex shedding. The effects of streamwise motion are also shown, including the increased phase coherence of the shedding via coordination of the shedding process and the ability to adjust formation time via streamwise acceleration. The latter was used to demonstrate a plausible explanation for the vortex pair formation process observed by some researchers by showing how the formation process affects the number of vortices generated per cycle.

# Contents

# List of Figures

# 1

# Introduction

Lost in the murky depths of prehistory, mankind first learned to use fluid-structure interactions. Perhaps it was to vibrate a reed to make music or maybe it was to flap wet clothing in the breeze to dry it faster. Presumably the nature of this coupling was unknown to prehistoric man, but by accident or observation, the various effects associated with fluid-structure coupling have shaped our history. Imagine if a stirring stick did not generate large amounts of turbulence or vibrating vocal cords did not produce sound.

Of particular interest here are couplings that introduce motion in the structure from oscillatory forces in the fluid. Here the story is more negative, since such events are associated with structural failure from fatigue loading. Under the relentless hand of fluid vibration, even seemingly durable steel can fail. The ubiquitous, and dramatic, example being the failure of the Tacoma Narrows bridge, where wind loading caused a bridge strong enough to bear the weight of many cars to be twisted and bent into failure. The study of such couplings has revealed that a wide range of mechanisms are involved. Some are quasi-steady, involving the changing lift characteristics of a structure as it bends in the oncoming wind. Some are due to unsteadiness already present in the fluid (like waves in the sea) interacting with the preferred modes of a structure. This thesis is concerned with interactions involving the naturally occurring vortices in the wake of a structure with the structure itself. Since these vortices impose a different pressure distribution than the ambient fluid, their presence leads to a change in the forces on the body. And when these vortices interact and move, these forces evolve dynamically. In particular, when these vortex motions have characteristic frequency near to the resonant frequencies of the structure, a feedback coupling the motion of the body to the motion of the wake can exist.

An important contribution to the science of flow-structure interaction came in 1878 with an observation by Strouhal that the vibrational frequencies of structures are proportional to the flow speed and inversely proportional to the diameter of the structure. This means not only that the vibrations are predictable, but regular. Hence there would be a characteristic vibration frequency associated with a given flow and structure, which is referred to as the Strouhal frequency (St). These frequencies are sometimes audible, leading to such phenomena as the Aeolian tones. Consequently one can presume that if this frequency were sufficiently close to the resonant frequencies of the structure, it could couple in a manner analogous to harmonic forcing of a spring-mass-damper system.

Once it was established that the wake has a characteristic frequency, the next stage was to show that this frequency came from vortex shedding. Benard (1908) and Kármán (1912) showed that the cylinder wake could consist of a periodic series of vortices. This connects the flow around the cylinder directly to the fluctuating forces. The Strouhal frequency exists because the cylinder sheds vortices periodically. Hence it could be deduced that the interaction of the flow with the body would directly produce the fluctuations.

The logical next step was to actually measure this interaction. Researchers like Feng (1968), Ferguson (1965), and others looked at the coupling of the vortices to the motion of cylinders attached to simple structures (like a spring & damper). When the frequency of the wake is near the natural frequency of the structure, a strong coupling response occurs, leading to fairly large amplitude oscillations in the structure. However, it was also found that this system exhibited non-linear behavior like hysteresis and frequency locking that introduced yet more interesting wrinkles to this problem. Other researchers like Den Hartog (1934), Bishop & Hassan (1964), Williamson & Roshko (1988), and Ongoren & Rockwell (1988) have studied the complementary problem, observing the response of the flow to simple harmonic motion. Such studies have led to a better understanding of the wake structures responsible for the induced motions. An interesting observation from this line of research is that both the wake and the forces appear to flip in phase (with respect to the cylinder motion) at a frequency near the Strouhal frequency of the stationary cylinder. (See Parkinson (1989), Bearman (1984), and Sarpkaya (1979) for an overview of the field.) Some of these important works will be discussed below in greater detail.

## 1.1 Observed changes in the fluid forces near Strouhal frequency.

By using the parameter space mapped out for freely vibrating cylinders, forced motion experiments could be carried out to approximate the

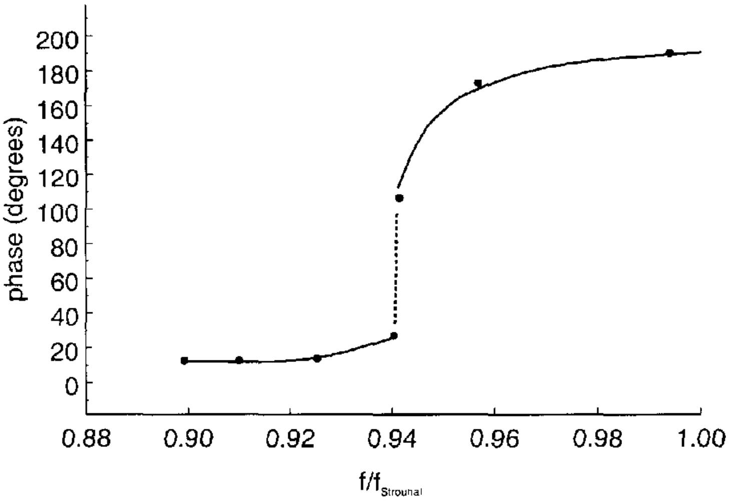

*Figure 1.1.1 - Phase relationship between the lift forces on the cylinder and its motion. Data from Bishop & Hassan (1964). Note axes are rescaled for consistency in notation.*

free vibrations in a controlled manner. By prescribing the motion of the cylinder, one can not only choose the point in parameter space to study, but study it with the sort of repeatability that the free-vibration experiments lack. One can also study regions of parameter space that freely vibrating cylinders do not reach. Not only were such experiments able to map out the force amplitude response of the wake, they were able to find the phase relationship. As shown in figure 1.1.1, there is a strong phase shift in the wake near the nominal Strouhal frequency. This change in phase is the equivalent of the vortices shedding from the opposite side; flipping the sign of the shedding vortex flips the direction of the resultant lift force. In other words, it appeared that one was able to flip the wake by changing the frequency of oscillation – perhaps a surprising thought.

Another important concept is best illustrated in free oscillation studies: lock-in. Lock-in is a situation where the wake appears to adjust and lock itself to the motion of the body. During lock-in, the dominant frequency of the wake will deviate significantly from the Strouhal frequency. In figure 1.1.2 data from Feng (1968), as published in Parkinson (1989), are reproduced. Shown is the main frequency of

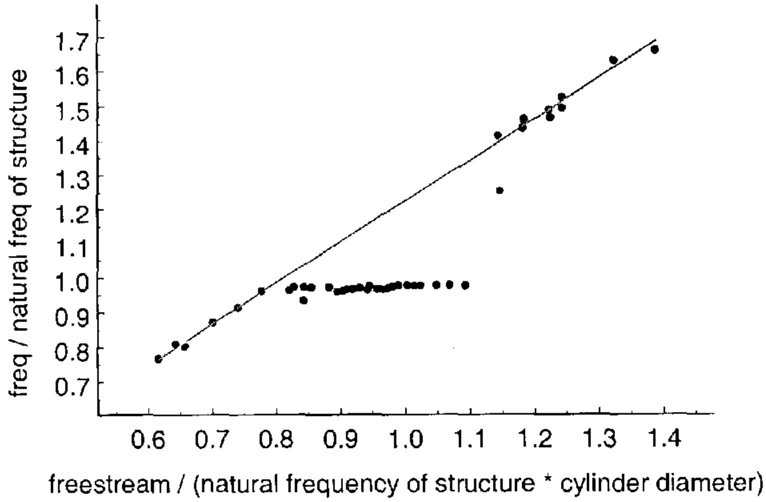

*Figure 1.1.2 - Wake frequency vs the natural frequency of the structure. Note the region where the wake frequency strongly deviates from the Strouhal line (solid line). Data from Feng (1968) via Parkinson (1989).*

the wake relative to the natural frequency of the structure. Within a certain range, the wake takes on the frequency of the structure; outside this range the wake continues to oscillate at the expected Strouhal frequency.

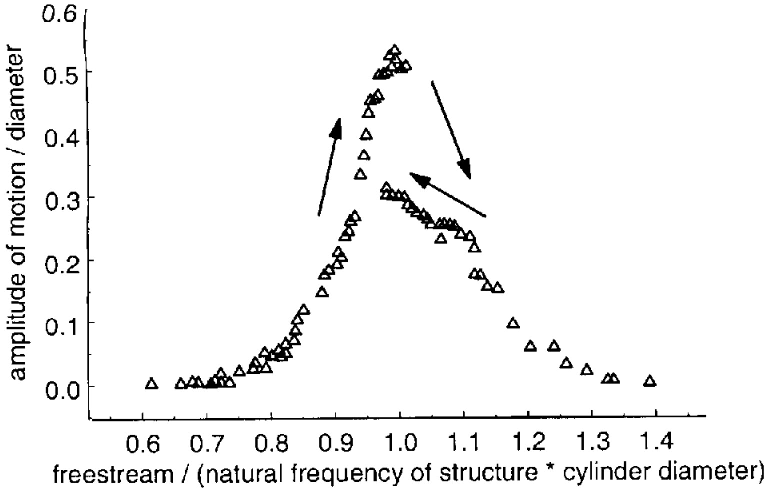

*Figure 1.1.3 - Amplitude of free oscillations in the lock-in range. Discontinuity results from hysteresis effects depending on the direction of survey in frequency. Data from Feng (1968) via Parkinson (1989).*

Similarly, figure 1.1.3 shows the amplitude response reported by Feng. (These data are for a cylinder considerably denser than the ambient fluid with low structural damping. The actual response varies with both damping and density ratios.) The range where the wake locks its frequency to the structure's natural frequency corresponds to the region where the cylinder amplitude is highest. (The discontinuity in the curve is due to hysteresis effects. Several researchers have reported two modes in the wake, where more than one amplitude is possible for a given frequency, depending on the frequency history.) The cylinder wake is shown to be "compliant," and hence the interaction region is wider than for a simple resonant oscillator. In an analoguous manner, the wake of a forced cylinder is also able to take on the frequency of the motion.

## 1.2 Observed changes in the wake near the Strouhal frequency.

Important clues to the origin(s) of the wake behavior were discovered through several flow visualization experiments. Previous experiments suggested that there might be a sudden change in the behavior of shedding near the Strouhal frequency, as if the wake changed modes in this region. After all, looking at both the hysteresis effects in the free vibration amplitude and the fairly sharp jump in phase for forced vibrations would suggest a state transition. A straightforward way to find this mode change is by using flow visualization. In 1988 Williamson and Roshko presented the results of an extensive survey of the amplitude vs frequency parameter space. In their experiment, a cylinder was towed along a prescribed path in a tank of still water and the wake was visualized using aluminum flakes on the free surface. Time lapsed photographs of the flake patterns revealed the positions of the vortices; from these, the vortex dynamics could be inferred. The vortex shedding from the cylinder indeed appeared to change modes, switching from two single vortices shed per cycle (the 2S mode) to two pairs of vortices shed per cycle (the 2P mode). Figure 1.2.1 shows the results of their survey near the region where natural vibrations are seen to occur. Hence it was assumed that the change in phase of the lift force was due to the changing from the 2S to the 2P mode and vice versa.

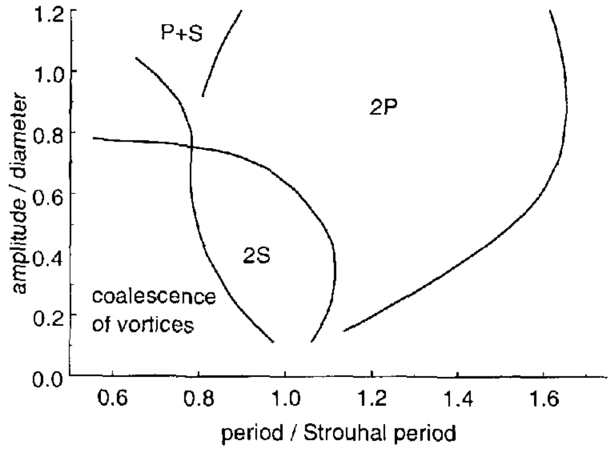

*Figure 1.2.1 - Wake modes for different motion parameters. From Williamson & Roshko (1988). 2S - two single vortices shed per cycle, 2P - two pairs, and P+S - one single and one pair.*

In 1988 Ongoren and Rockwell performed a set of experiments more closely examining the issue of phase in the wake. In these experiments, a pulsed hydrogen bubble visualization system was used in a free-surface water channel. Their experiments detailed the switching of the phase of vortex shedding as the transition frequency is crossed by showing pictures of the vortices at constant relative position, but different frequencies (e.g., pictures of the wake when the cylinder was at the upper-most point of its motion). They noted that the phase of vortex shedding does indeed appear to switch as the frequency crosses the Strouhal frequency. They do not seem to find the 2P mode, although this is perhaps due to their relatively low oscillation amplitude (only 0.13 diameters).

### 1.3 Objectives and scope of this work.

The main focus of this thesis is to study the interaction between the wake and the body for natural motions. Observations, both by ourselves and others, have implied that an oscillating body should have both transverse and streamwise motions. This is not entirely surprising as researchers have long known that there are flucuations in both the drag and lift forces. Consequently, the primary area of interest is the effect of adding the streamwise motion to the simpler case of transverse motions. However, to understand the vortex interactions, it is also important to understand the formation process of vortices in general. To that effect, there will first be a discussion of a different problem: the starting flow around an initially stationary cylinder. This flow is generated by quickly starting a cylinder up to a constant final velocity. This presents a clean case of vortex formation and will assist in the discussion on formation in the oscillating case. A final area of interest is the phase change around the transition frequency, when the lift force switches nearly 180° in phase with respect to the cylinder motion. Understanding the mechanism which drives this phase change requires the melding of both oscillating and starting flows.

# 2

# Theory

The following is a brief discussion of the underlying theories and postulates for this work. First is a discourse on the selection of parameter space. Following that is a short section on the vortex formation time as it was first applied to the vortex ring and the starting cylinder. Then this idea is expanded to cover the oscillating cylinder, which in some sense is actually the inverse problem. (The formation time is known – the Strouhal period – but not how, or if, it plays a part in the oscillating cylinder flow.) Lastly there will be a section on the force deduction technique used to extract the force information from the experiments.

### 2.1 Parameters and parameter space.

The oscillating cylinder flow is a competition between the motion of the cylinder and the wake behind it. The parameters of this flow have to define both the motion and the fluid. There are three fluid dynamic parameters – freestream velocity(U), cylinder diameter(D), and fluid viscosity($\nu$) – and five motion parameters – streamwise/transverse amplitude ($A_x$, $A_y$), streamwise/transverse frequency ($f_x$, $f_y$), and relative phase($\phi$). These are further lumped into six main parameters: non-dimensional amplitude ($A_x/D$, $A_y/D$), relative transverse frequency to stationary cylinder wake frequency ($f/f_{St}$, where $f_{St}=St \cdot U/D$), frequency ratio ($f_y/f_x$), phase($\phi$), and the Reynolds number ($Re=UD/\nu$). (Streamwise is the direction of the freestream flow and transverse is the direction normal to both the freestream and the long axis of the cylinder.)

Using past experience and data from natural oscillations this collection of parameters was narrowed. Since the goal is to understand natural vibrations, values were chosen to best mimic the motions of a freely vibrating cylinder. Observations suggested that the motion should be a figure-eight; this would mean that $f_y/f_x=2$. This is also expected since it is well established that the drag frequency is twice that of the lift. Further, the patterns tended to be of greater extent in the transverse than streamwise direction; this suggests that $A_x$ should be much less than $A_y$. Free vibration cases suggest that the motion frequency must be very near $f_{St}$ for the wake to lock to the cylinder.

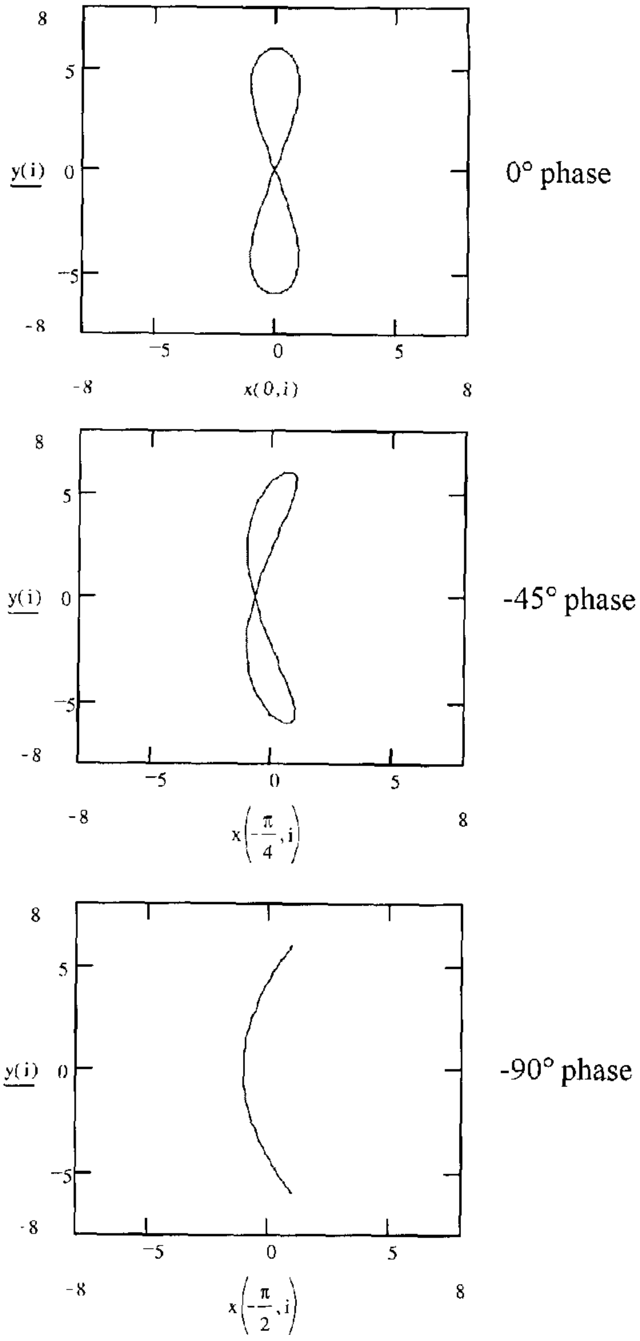

*Figure 2.1.1 - Examples of figure-eight patterns as a variation of relative phase between the streamwise and transverse motions.*

This would leave Re and $\phi$ as free parameters. Previous studies would suggest that there is little sensitivity to Re in the range of 500-3000 (Williamson and Roshko, 1988). After all, barring a Reynolds number dependent transition, the local flow is expected to be strongly dominated by the motion. Limitations of the experimental setup put the Reynolds number in the range of 800-1500, so that is of little concern. Instead the focus is on relative phase. Figure 2.1.1 shows figure-eight motions with different phases. A wide range of patterns is possible even if only phase is varied. Again appealing to experience, phases between 0 and -45 degrees are considered (based on the shape and direction of motion). Actual run conditions are listed in appendix D.

### 2.2 Vortex formation time.

Although researchers were aware that the manner in which vortices were produced would influence the final vorticity field, the detailed nature of this process was not studied until fairly recently. A particularly clean flow to study formation is the vortex ring, a flow which consists of one vortex whose ends are connected together to form a ring. A common example of vortex rings is the smoke ring. By trial-and-error, researchers found that generating the rings quickly led to clean, thin rings, and slowly led to messier, thicker rings. However, it was not until Gharib, et al. (see Gharib, Rambod, & Shariff, 1998) that this process was well understood. As is frequently the case, nature had a more interesting version of formation than had been appreciated. In their experiment, a piston-in-cylinder arrangement was used to push a specified slug of fluid into a still tank. Using digital particle image velocimetry, the formation, growth, and pinch-off processes of the vortex ring were followed as a function of time. Scaling time by the running average piston speed and piston diameter, this results in a non-dimensional time of

$$t^* = \frac{t\overline{U}}{D} = \frac{t}{D}\frac{1}{t}\int_{t_0}^{t} U dt' = \frac{S}{D} \qquad \text{(eq. 2.2.1)}$$

which, incidently, is also the number of diameters the generating piston travelled (S). This type of scaling strongly reduces the dependence of the non-dimensional time on the acceleration history at the beginning of the run. As expected, at short time the rings are clean and compact. The surprising discovery was that at long time (greater than four) the rings did not grow indefinitely. The rings appeared to saturate, with the left-over circulation ending up in a trailing jet-like structure. It was found that no matter how long the piston was travelling, the maximum circulation in the ring occurred around $t^*=4$.

Afterwards, a similar experiment was proposed using a circular cylinder as a vortex generator. In this flow, a pair of symmetrical and parallel vortices are generated at early time. This pattern eventually breaks down and leads to the periodic vortex shedding mentioned in the introduction. The question that was posed was whether or not the starting cylinder had a similar saturation behavior as the vortex ring. Like the vortex ring, most studies on this flow are for early time [see Bouard & Coutanceous (1980), Honji & Taneda (1969), and Koumoutsakos & Leonard (1995)], where the vortices are clean and symmetrical. Time is scaled in a similar fashion, substituting the cylinder speed and diameter into equation 2.2.1. The experiments were conducted for a variety of final Reynolds numbers and ramp profiles. The circulation of the vortices was tracked in time and compared to the level of circulation of the vortex that is the first to shed. Coincidently, the starting cylinder turned out to have the same formation time as the vortex ring, around four diameters. These experiments will be discussed in greater detail in §4.

### 2.3 Formation time for the oscillating case.

Since the starting case showed that cylinder wake vortices also had a characteristic formation time, it seemed natural to see if a similar time scale exists for the oscillating case. However, the problem is an inverse one, since we already know the time scale: the Strouhal period defines the natural time at which shedding occurs. Some characteristic formation must be setting the Strouhal period since the stationary cylinder has no way to define the period by itself. The flow naturally settles to a constant formation time. Therefore, the question becomes how many diameters a cylinder travels per shedding cycle when the cylinder is oscillating. For frequencies near Strouhal, it is known that the wake locks to the motion frequency; therefore, we can expect that there will be a variation in formation time with different motions.

Plotted in figure 2.3.1 is a comparison of different motions. The abscissa is the relative time (time/period) and the ordinate is the number of diameters travelled. To compute these curves, the velocity of the cylinder is integrated forward in time to determine the number of diameters travelled. For example, if one starts with a cylinder moving at steady speed with a purely transverse oscillation,

$$u_x = U_\infty \qquad \text{(eq. 2.3.1)}$$
$$u_y = 2\pi f\ A \cos(2\pi f\ t)$$

where A & f are the amplitude and frequency, respectively, of the motion. Taking the velocity magnitude,

$$|\mathbf{u}(t)| = U_\infty \sqrt{1 + (2\pi\alpha \frac{St}{D} A)^2 \cos(2\pi\alpha f_{St} t)^2} \qquad \text{(eq. 2.3.2)}$$

where St is the Strouhal number, and $\alpha \cdot f_{St}$ is the frequency relative to the Strouhal frequency. The equivalent formation time is

$$FT = \frac{1}{D}\int_0^t |u(t')| dt' \qquad \text{(eq. 2.3.3)}$$

For the oscillating case, average velocity was numerically integrated. The straight, solid, black line indicates the pathline of the non-oscillating cylinder. By definition, the point where this line hits time=1 defines the number of diameters the stationary cylinder travels per shedding cycle. What is interesting to note is, in spite of the transverse excursions, the oscillating cylinder can actually shed in fewer diameters because the actual time of integration decreases. If the same kind of vortex behavior as the vortex ring or the starting case exists, for formation times greater than the Strouhal period, the wake must somehow adjust itself to accommodate the extra circulation. Whereas the shortened time of the higher frequency cases can be understood as foreshortened vortex shedding, something more drastic must occur for the low frequency mode.

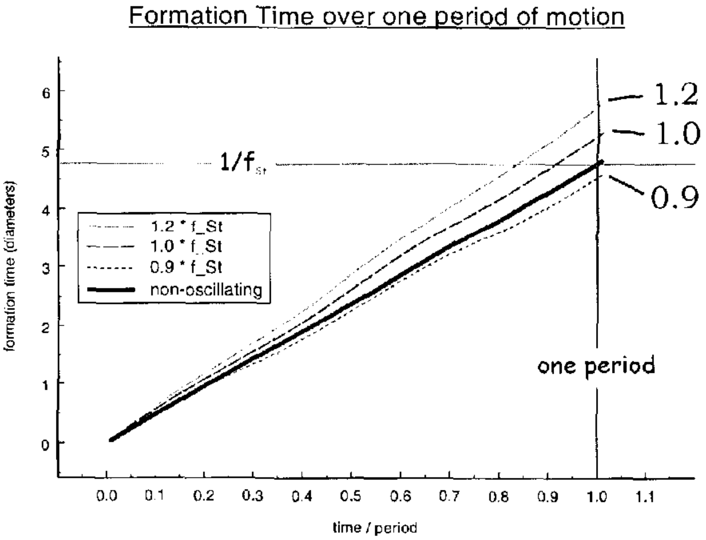

*Figure 2.3.1 - Approximate formation time for a series of different cylinder motions.*

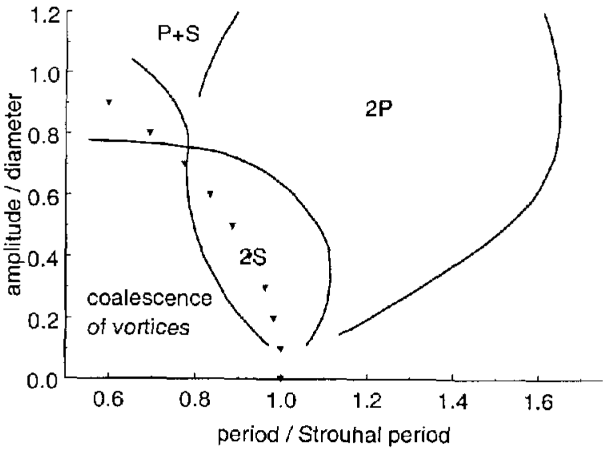

*Figure 2.3.2 - Comparison between the suggested critical period and the wake mode map from Williamson & Roshko (1988).*

The suggested critical period is plotted on the Williamson & Roshko mode map in figure 2.3.2. The discrepancy between these points and the line dividing the 2S & 2P regions is likely due to the absence of accounting for which sign of circulation is generated at which part of the motion. Unlike the starting cylinder or the vortex ring, a component of the cylinder velocity changes sign. The cylinder's transverse velocity changes direction, which means a component of the generated circulation changes sign. However, compensating for this is beyond the scope of this model since one needs to know the details of the shedding behavior to predict how much opposite signed vorticity will be injected into the vortex. Also, the transition occurring at the critical time might not be the same transition that occurs between the 2S and 2P modes. What is clear, however, is that one should expect a formation time type transition in this region of parameter space.

### 2.4 Force deduction.

In order to link the wake to the cylinder motion, the forces exerted by the flow onto the cylinder need to be measured. The first choice to measure these forces was a force balance. However, it is important to develop an independent measurement technique to both verify and complement the balance. The force balance has two primary weaknesses: it is an integral measurement (along the span) and it is often noise limited at low force levels.

Since the force balance is attached to the entire cylinder, the force it measures is averaged over the entire span of the cylinder. Because real cylinders are of finite length, they must necessarily end somewhere. The manner in which the cylinder ends affects the overall forces measured since the cylinder is no longer purely two-dimensional. And the shorter the cylinder, the greater the effect of the ends. Hence it is preferable to measure the force at a station where the flow is as two-dimensional as possible. (See Szepessy & Bearman, 1992.)

Force balances are inherently limited at low force levels. Most balances are designed to measure displacement, from which forces can be inferred using basic solid mechanics. This means that one needs either very high resolution displacement measurements or relatively large displacements. Neither situation is acceptable in this case. Since this cylinder is undergoing forced oscillations, there will be unavoidable vibrations in the system that will be measured as noise if one relies on high displacement resolution. And, of course, too much parasitic displacement in the balance corrupts the intended motions. As a result, it was deemed important to have a complementary technique that is not affected by the dimensional quantity of force involved; whether it be a nanogram or a pound, no large change in force measurement quality should be seen.

As a result, a force deduction technique developed by Noca (1997) was used. Noca described a set of techniques by which the forces on a body could be deduced from a set of velocity measurements. Previous fluid mechanical measures of force required knowing either the pressure field around the body (direct integration method) or the entire vorticity field (impulse method). The main equation is quoted below:

$$\begin{aligned}\mathbf{F} = &-\frac{1}{N-1}\frac{d}{dt}\int_{V(t)}\mathbf{x}\wedge\omega\, dV + \oint_{S(t)}\hat{\mathbf{n}}\cdot\Theta\, dS \\ &-\frac{1}{N-1}\frac{d}{dt}\oint_{S_b(t)}\mathbf{x}\wedge(\hat{\mathbf{n}}\wedge\mathbf{u})\, dS\end{aligned} \qquad \text{(eq. 2.4.1)}$$

$$\begin{aligned}\Theta = &\frac{1}{2}u^2\mathbf{I} - \mathbf{u}\mathbf{u} - \frac{1}{N-1}(\mathbf{u}-\mathbf{u}_s)(\mathbf{x}\wedge\omega) \\ &+\frac{1}{N-1}\omega(\mathbf{x}\wedge\mathbf{u}) \\ &+\frac{1}{N-1}[\mathbf{x}\cdot(\nabla\cdot\mathbf{T})\mathbf{I} - \mathbf{x}(\nabla\cdot\mathbf{T})] + \mathbf{T},\end{aligned}$$

where T is the stress tensor (including viscous terms), *N* is the dimension of the flow, $u_S$ is the motion of the body, $\hat{n}$ is the surface normal on the control volume, and integrals are taken on a control volume that surrounds the bluff body. Variations are also described in his work, depending on whether one wishes to take more volume or surface integrals to compute the various terms. In effect, this deduction method algebraically converts the pressure terms into velocity derivatives. By removing the pressure term one could thus convert velocity field measurements directly into the forces on the body. Furthermore, since the velocity measurements are sectional, the forces are also sectional. DPIV measurements are typically averaged over 2-3 millimeters, compared to cylinder diameters on the order of 2-2.5 centimeters and cylinder lengths on the order of 40-50 centimeters in these experiments. And the accuracy is controlled by the velocity measurements, and not the level of force. Consequently, the actual force levels are not directly important. The technique is mostly limited by the ability to measure velocities so forces of micrograms or kilotons can be measured to similar accuracy.

As noted in Noca, et al. (1997), standard particle image velocimetry (PIV), the measurement technique of choice for this experiment, is a bit lacking in both temporal and spatial resolution. For a fully resolved Navier-Stokes computation the Noca method reproduces the forces calculated by more traditional techniques. Resolving the thin boundary layers on the cylinder is yet beyond the capability of current camera technology (1-5 millimeter objects in a 10 cm field of view), as well as the frame rates required to keep pace with the rapidly varying vorticity fields (order 100 Hz sustained for more than minute). Rather than settling for a velocity field limited force deduction strategy, a time averaged force deduction technique was devised. By trading temporal resolution for accuracy, it was hoped that these resolution limits could be avoided.

The first step was to convert Noca's formulas to a Reynolds averaged form. Here one partitions the flow field into stationary and fluctuating components; in a sense, a division between laminar and turbulent components. The quantities are listed as equation 2.4.2, where overbars represent stationary quantities and primes represent fluctuating quantities around a zero mean.

$$\begin{aligned} u &= \bar{u} + u' \\ v &= \bar{v} + v' \\ \omega &= \bar{\omega} + \omega' \end{aligned} \qquad \text{(eq. 2.4.2)}$$

By substituting equation 2.4.2 into equation 2.4.1., and averaging the resulting equations over time, the formulas reduce to those in equation 2.4.3. (Note that by definition, the average of a fluctuating quantity by itself is defined to be zero.)

$$\bar{\mathbf{F}} = \oint_S \hat{\mathbf{n}} \cdot (\bar{\Theta} + \Theta')\mathbf{dS} \qquad \text{(eq. 2.4.3)}$$

$$\begin{aligned} \bar{\Theta} + \Theta' = {} & \frac{1}{2}(\bar{\mathbf{u}}^2 + \mathbf{u}'^2)\mathbf{I} - \bar{\mathbf{u}}\bar{\mathbf{u}} - \mathbf{u}'\mathbf{u}' - \frac{1}{N-1}(\bar{\mathbf{u}}(\mathbf{x} \wedge \bar{\omega}) + \mathbf{u}'(\mathbf{x} \wedge \omega')) + \\ & \frac{1}{N-1}(\bar{\omega}(\mathbf{x} \wedge \bar{\mathbf{u}} + \omega'(\mathbf{x} \wedge \mathbf{u}')) + \frac{1}{N-1}(\mathbf{x} \cdot (\nabla \cdot \bar{\mathbf{T}})\mathbf{I} - \mathbf{x}(\nabla \cdot \bar{\mathbf{T}})) + \bar{\mathbf{T}} \end{aligned}$$

This form gives the time averaged forces on the cylinder. Although one has lost all information about when the forces occurred, this formulation would be much more accurate for a given flow since the average quantities are considerably easier to resolve and measure than the instanteous ones. It would seem that this is of limited use for oscillating cylinders since without the dynamic force data, it would be difficult to connect the wake back to the body. After all, one already knows that the time average lift should be zero on symmetry arguments, and confirming

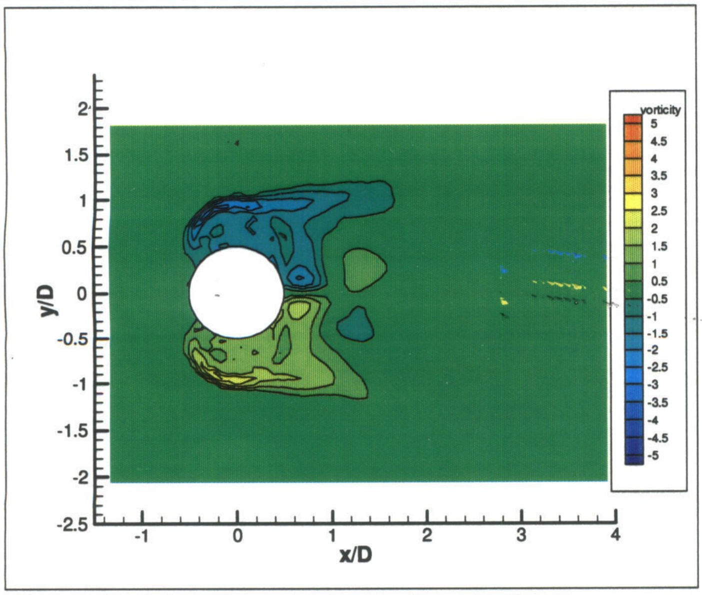

*Figure 2.4.1 - Time averaged vorticity field of a sample flow.*

that would not be illuminating.

However, this method of averaging is a bit simplistic, since the cylinder's motion is known. Figure 2.4.1 shows an example of an average vorticity field. The overall average field would translate into overall average force; but one can average more intelligently. For example, one could average all the fields when the cylinder is in the upper half of its motion separately from when it is in the lower half. This results in the pair of fields shown in figure 2.4.2, along with their respective fluctuating components (not shown). If one computed the forces here, one would get the average force in the upper half of the cylinder motion and the average force in the lower half of the motion. Dividing into four parts,

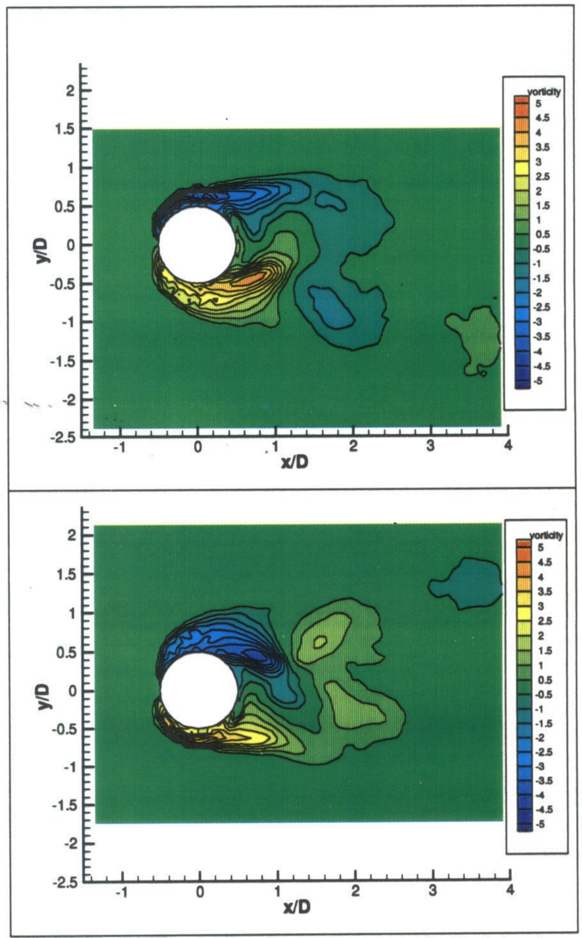

*Figure 2.4.2 - Sample flow subdivided into two parts. Upper - cylinder in upper half cycle. Lower - cylinder in lower half cycle.*

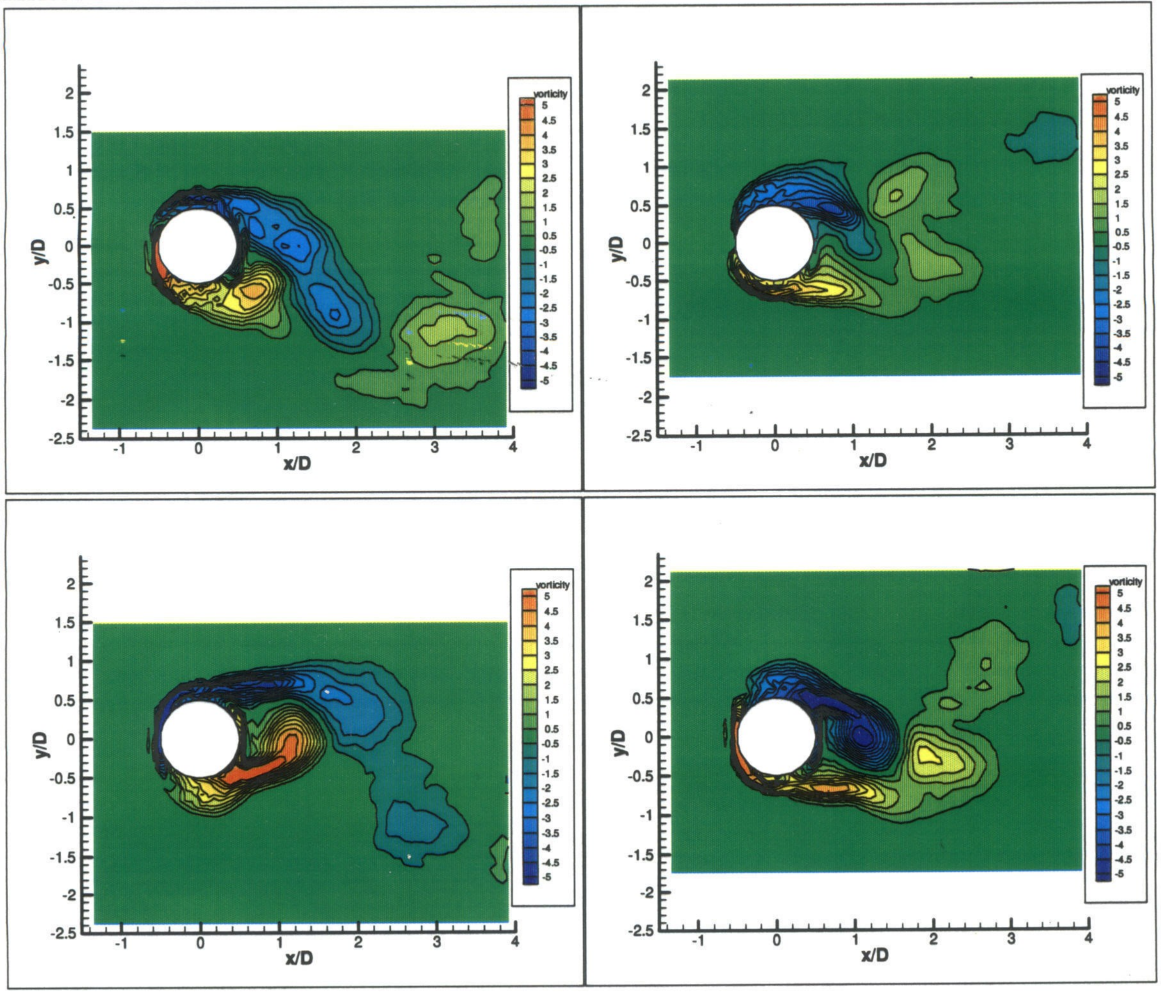

*Figure 2.4.3 - Sample flow subdivided into four parts according to phase.*

one can continue this process, as shown in figure 2.4.3. In fact, by using information about the cylinder motion in this manner, one can reconstruct a phase averaged force history for the cylinder. By dividing the flow field into $n$ parcels in phase, one would get a set of $n$ force values averaged over $1/n$ of the cycle. Figure 2.4.4 shows this progression from 1 to 2 to 4 to 12 partitions. As a result, one can now compute, with considerably better confidence, the forces on the cylinders at the various times in phase, and hence reconstruct the total force history.

An alternate view of the process is to "pretend" that the long term average of a flow happened to look like one of the phase averaged fields, with a fluctuating component associated with it. If such a flow field could exist, one could measure its time average force as well. In fact, with greater subdivision in phase, one actually approaches the original idea of "velocity = steady part + random fluctuating part" more closely as the phase averaged velocity fields look more like the instantaneous velocity fields. At no time does the flow field resemble figure 2.4.1, but after many subdivisions, the resemblence is very close. With either path, one can safely and confidently deduce the forces on the cylinder, and match them to the appropriate part of the phase.

This phase averaged force method does not account for inertia. By averaging in this manner, information about how the cylinder moves from point to point is lost. Fortunately, from the proscribed motion, it is possible to reconstruct the inertial (or added mass) forces on the cylinder from the known acceleration history. (For the circular cylinder, added mass is equal to the mass of the displaced fluid. Hence one would add an added mass * cylinder acceleration to the deduced force.) This information, combined with the phase averaged force results, completes the picture of sectional force on the cylinder.

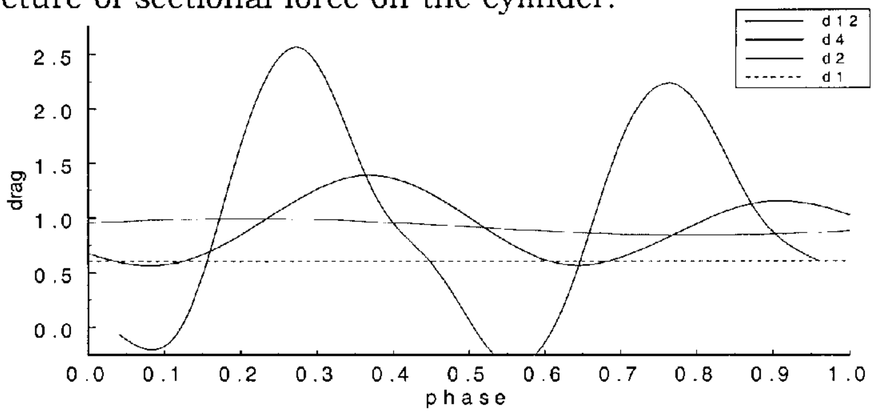

*Figure 2.4.4 - Study of the variation of the phase averaged drag with the number of subdivisions in phase. Shown without inertia force added in.*

# 3

# Experimental Setup

The most difficult obstacle in this experiment was the need for simultaneous acquisition of data. This meant that the motion controller, the video system, and the data acquisition systems all had to work synchronously. To maximize confidence in understanding how the wake dynamically affects the cylinder, all of the data needed to be taken in a dynamically relevant manner.

This synchronicity also affects the choice of run parameters. It was necessary to compromise between the traverse motion speeds, the video acquisition speed, and the force balance sensitivity. Given the weight of the traverse and the motor power, there is a practical limit to the acceleration that could be generated, which limits the maximum frequency of the cylinder motions. The video rate also limits the maximum speed since sampling the velocity field is forced to 15 Hz; Nyquist sampling would limit the motion to 7.5 Hz. In contrast, the force balance wants high speeds since the forces on the cylinder scale with the dynamic pressure (which scales with the square of the freestream velocity). These issues then necessitated the use of a fairly low freestream speed: fortunately, the water tunnel was able to provide the necessary low speeds. However, it required the force balance to operate at low force levels.

Lastly, the optical system had challenges in terms of shadows and parallax. The force deduction technique requires data in a control volume that completely surrounds the cylinder. Unfortunately, the cylinder itself tends to prevent this by casting a shadow which prevents imaging a region of the flow field. Furthermore, the need to image around the cylinder brings up a parallax problem as the near end of the cylinder would appear disproportionately large in the image, blocking the view of the region near the cylinder at the imaging location. These issues are not solvable, but can be mitigated to a satisfactory degree.

### 3.1 Two-axis traversing system.

The primary requirements for a traversing system were two-axis motion, feedback control, smooth motion, and fastest possible traversing speeds. A schematic of the traversing system is shown in figure 3.1.1. Although a two-axis traverse is easy enough to obtain, it was more challenging to find a traverse with fast motion in both directions. The added weight of the second axis usually meant that systems would not be very fast – or outrageously expensive. For example, Aerotech, the company from which the traverse was purchased, also sold a two-axis linear motor system designed for the semiconductor industry. This system was more than twice as fast as the system used here, but at a price exceeding $100,000. The need for both high torque (to overcome the inherent weight of the system) and high speed suggested the use of DC brushless motors, noted for their relatively high torque and flat torque curve. Brushless servo motors could also deliver smoothness, since they wouldn't have the inherent vibrations that stepper motions have. The traverse chosen for this work was an Aerotech ATS700015-U-TB system, using two Aerotech BM250-MS-

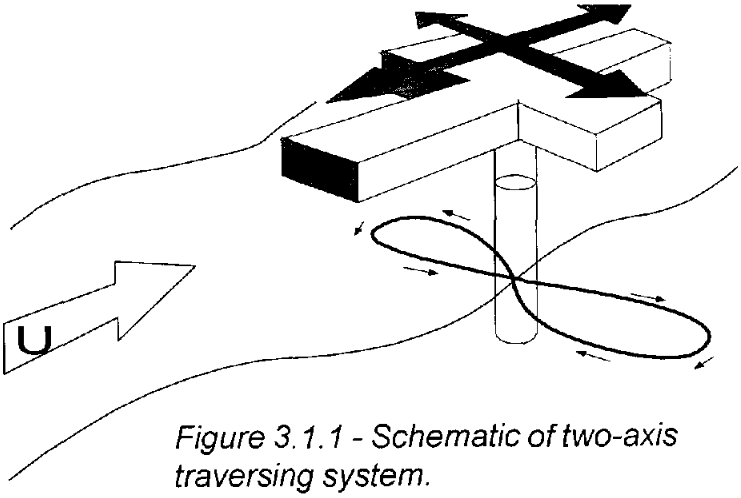

*Figure 3.1.1 - Schematic of two-axis traversing system.*

E1000H DC brushless motors and a timing belt between the motor and the platform. The timing belt was necessary for the speeds we needed since a lead screw transmission would be too slow and have too much friction. As an added benefit, the timing belt also further helps reduce vibrations since the belt will absorb some high frequency vibrations. The traverse also came with a 5:1 gear reduction on the streamwise traverse to help overcome the added weight of the transverse axis.

This system was connected to an Aerotech Unidex 500 servo controller system using Aerotech Unidex 500 MMI controller software. The software allowed programmable access to the motion controller system, simplifying the task of prescribing the motion. The Unidex 500 board is connected to a pair of Aerotech BA20-160 power amplifiers through an Aerotech BB501 breakout board, which also handles the feedback signals from the motors. The Unidex 500 system can also output an internal signal to the BB501 for diagnostics; this feature was used to output the position of the traverse. The instantaneous position could thus be measured synchronously by the data acquisition (DAQ) system.

### 3.2 Force balance.

The force balance was probably the single most problematic subsystem in this experiment, primarily due to the low levels of force that needed to be measured. It seemed the best compromise between lightness, simplicity, and sensitivity was to use a strain gage network directly on the cylinder holder. The strain gages would measure the forces between the cylinder and traverse. Knowing the generated motion, the forces on the cylinder can be backed out. At first, it was difficult to get the necessary sensitivity to measure the one to five gram forces without significant deflections. Early versions of the balance were plagued by

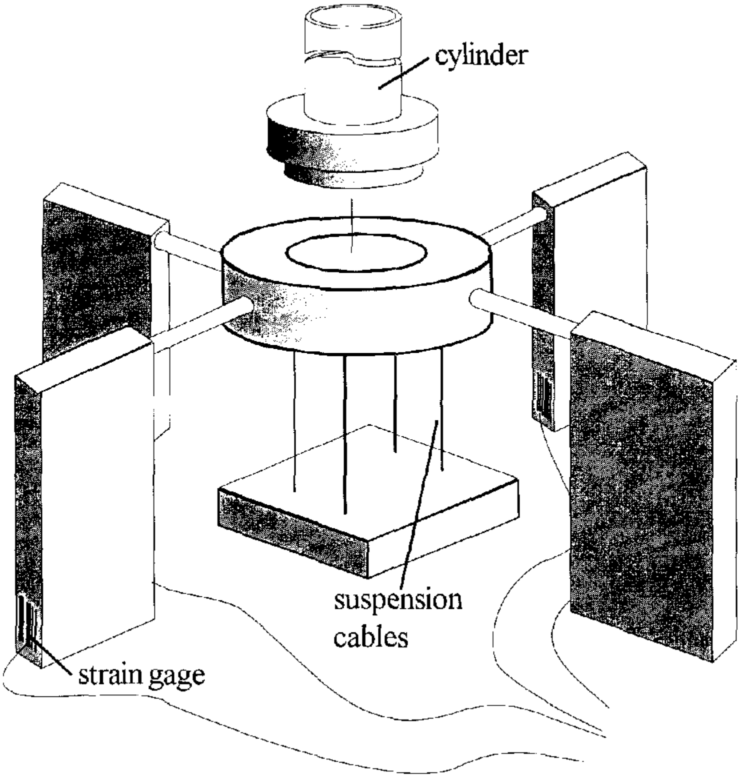

*Figure 3.2.1 - Schematic of cylinder holder and strain gage balance. Note: balance is mounted upside down in use with the cylinder pointing downward.*

excessive internal stiffness. This problem was eventually solved with the use of a cable suspension system. The test cylinder is mounted to a ring which is suspended from the traverse by four cables. This system provided low resistence to motion in the plane parallel to the ground, while maintaining excellent stiffness in the normal direction. The use of four cables ensures that the cylinder will deflect laterally without tipping.

The other main source of problems was electronic noise. As mentioned, the force balance was situated between the cylinder and the traverse. This meant the strain gages (operating in the millivolt range) were near the servo motors driving the traverse (operating at tens of volts and several amps). The noise from the motors could completely drown out the strain gage signals. Several measures were taken to minimize this interference. First the high power cables from the power amplifiers to the traverse motors were shielded and grounded. Second, the signal cables from the balance were switched to shielded twisted pair cabling, with the shield held to instrument ground. Lastly, care was taken to ensure that the power and instrumentation amplifiers had separate power sources to minimize crosstalk through a common ground.

These signals were amplified and filtered before being sent on to the DAQ system. A pair of Stanford Research SR560 instrumentation amplifiers – one per axis – were used, typically at a gain of 5000 to put the strain gage signal in the 1-2 volt range. The onboard filters were generally set for low-pass at 3 Hz. (Signals were in the 0.5 Hz range.) The strain gages were powered with a Hewlett-Packard 6236A power supply at 5 volts. These signals were measured and stored with a SuperScope II system using a MacADIOS II DAQ board in a Macintosh computer at 12-bits resolution and 1 kHz sampling. (This high sampling rate was used to resolve the laser firing rate. The timing generator would send out 5 ms wide pulses to tell the lasers when to fire.)

### 3.3 DPIV system.

Aside from optical issues, the Digital Particle Image Velocimetry (DPIV) system was the most reliable sub-system, providing time-resolved velocity field data over several cycles of motion. Simply put, DPIV relies on cross-correlation to infer local velocity from particle displacement. By

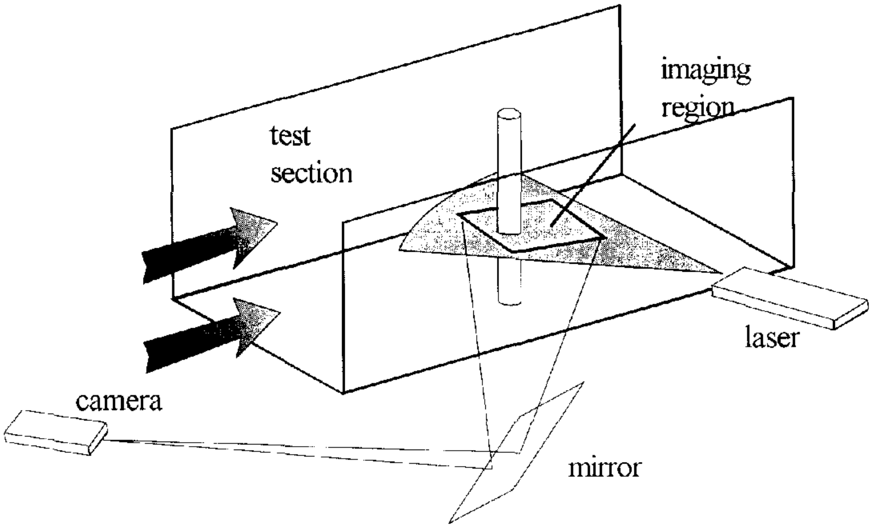

*Figure 3.3.1 - Schematic of PIV setup. Laser shines from the side of the test section and the camera looks from underneath, via the mirror. A thin-walled glass cylinder is used to allow imaging on all sides of the cylinder.*

illuminating a particle laden flow with a laser sheet, one can obtain a series of images of instaneous particle positions. By cross-correlating small windows of the images, one can then find the local displacement field, which can then be converted into the local velocity field by appropriately scaling. (See Willert & Gharib 1991 for more details on the workings of DPIV.) The flow was seeded with 40 micron silver-coated glass spheres (Potters Industries Conduct-O-Fil). These particles were slightly bouyant in water. At the low tunnel speeds of this experiment, this slight bouyancy was used to increase the particle seeding density in the test section. If the particles had been slightly denser than water, they would have settled into the return section instead. A schematic of the optical setup is provided in figure 3.3.1.

Illumination was provided by a NewWave MiniLase III pulsed Nd:YAG laser with the PIV head mounted on a Keuffel & Esser 9092 tripod. The Nd:YAG provides not only excellent brightness, but a very short pulse duration (on the order of 9 nanoseconds). This is more than sufficient for freezing the flow field, ensuring that the instaneous particle positions are recorded. The sheet forming optics – consisting of one cylindrical lens – were mounted onto the same bracket that fixed the laser head to the tripod. The tripod was approximately 1.5 meters to the side of the test section, illuminating the flow field primarily from the wake side. The images were taken with a Pulnix TM-9701 CCD video camera. The camera was mounted on a Slik 300DX tripod approximately five meters upstream of the test section and one meter to the side. The camera was rotated on its tripod mount so that the image was aligned with the freestream. The images were subsequently recorded onto a Sony LVR-5000A laser disc system. The images were then digitized with a Coreco

TCi Ultra-II board for processing into velocity.

To minimize the shadowing effect, thin-walled glass cylinders were used. These models are nearly transparent in the water, leaving only a slight darkening on the shadow side of the cylinder. To further reduce shadows, a mirror is placed on the opposite side of the water tunnel to fill in the shadow. Since the side-scatter efficiency is fairly low, there is plenty of light power for the mirror to redirect into the flow. The resulting images show almost no variation in light sheet intensity due to shadowing. In some cases the cylinder is only visible in the images because of the low seeding density of the fluid inside the model.

To minimize parallax issues, a long focal length lens was used, allowing the camera to be placed as far from the light sheet as possible. Ideally, a telecentric lens should be used to give, in effect, a viewpoint at infinity. However, a telecentric lens with a large enough field of view is prohibitively expensive. Typically the field of view of a telecentric lens is directly related to the size of the front element and the field of view is on the order of four to five inches wide. Using a Tamron 300 mm f2.8 lens on a CCD camera (equivalent of more than 800 mm on a 35mm camera) allowed the camera to be placed on the order of six meters from the light sheet, which is a fair compromise between distance and price. To get this kind of optical path length, it was necessary to place a mirror under the tunnel to turn the light path parallel to the floor. The mirror was adjusted relative to the cylinder: by adjusting the focus on the camera, one can readily see the angle of the optical system with respect to the cylinder by noting the relative positions of the two ends of the cylinder. The mirror and tripod were adjusted until the bottom and top of the cylinder were coincident. The residual parallax error is very small, with the bottom of the cylinder barely larger than the cylinder at the light sheet.

The DPIV system was synchronized with the use of a time-delay generator. A custom timing box was used to synchronize the lasers to the camera's video signal to within one microsecend. By adjusting the timing of the laser firing, the effective time between successive images can be reduced to several microseconds instead of being fixed to the video rate of 33.3 milliseconds. The images were then synchronized to the DAQ with the use of an LED placed inside the hollow cylinder. After the run is started, the battery powering the LED is switched off. By comparing when the image of the LED disappears with the time the battery is switched off, one can readily synchronize the two subsystems. Combining that time difference with the laser firing signal from the time-delay generator gives the relative time between the PIV data sets and the DAQ system.

Determining the position of the cylinder is a two step process. First the position information from the motion controller is fitted to determine the period and phase relative to the DAQ time. Then the location of the cylinder in the images is measured for several instances. This is done by measuring the intersection of perpendicular bisectors of four points on the surface of the cylinder. Thus one has the position of the cylinder in image coordinates as a function of real time, and hence one knows where the cylinder is, how fast it is moving, and in which direction it is moving. These data are used to fill in the location of the cylinder in the velocity field with a slug of fluid moving in the appropriate manner.

Estimates of the resolution are as follows. Spatial resolution is approximately 16 pixels. Through the use of the Hanning window and window shifting, the effective window size is reduced from 32x32 pixels to about 16x16 pixels. (Spatial filtering is a custom DPIV procedure developed as part of this thesis.) This corresponds to approximately 0.16 diameters in a window. Temporal resolution is fixed to 15 data sets per second, which corresponds to approximately 33 data sets per period.

### 3.4 Water tunnel.

Initially the experiment was scheduled to run in a free surface water tunnel in the basement of Guggenheim. Due to construction and renovation, the experiment was repatriated to a new water tunnel facility in the sub-basement of Keck, where our gracious hosts provided space in the hydraulics laboratory. In comradely fashion this new facility took more than a year to construct and debug, including several replumbing efforts and the addition of a low frequency wave damper over the intake plenum. However, the move proved beneficial because the new tunnel is capable of running at substantially lower speeds. For example, with transverse motions around 0.5 Hz and a one-inch cylinder, a freestream speed on the order of five cm/sec is required, well within reach of the Keck water tunnel. In contrast the Guggenheim tunnel's lower practical limit was on the order of nine to ten cm/sec.

This water tunnel has an open free surface which is used for mechanical access. The traversing system was placed above the tunnel with the cylinder piercing the surface. The free surface functions as clean boundary condition. Since vortices tend to connect to the free surface normal to the surface (to satisfy the no shear condition at the surface), the flow field tends to be more two-dimensional near the surface. One might expect J-shaped vortices from a surface piercing cantilevered cylinder, with one end emanating from the free end and terminating normal to the free surface. The PIV light sheet was biased towards the surface to take advantage of the more two-dimensional flow. Typically, the sheet was placed about 75% of the distance from the floor of the tunnel to the free surface. The free end was placed at the edge of the boundary layer on the tunnel floor; this seemed to provide the best pressure matching condition, which in turn minimized axial flow up the cylinder from the free end.

This facility also has good optical access with large transparent windows on the sides, underneath, and downstream. For PIV, the laser was placed on the side with the sheet parallel to the free surface and the sheet was viewed from underneath. The side laser allowed the shortest optical path through the water, which gave the least attenuation through the particle seeded water. The area underneath the test section is large enough to place a large mirror (12 inch square) beneath the model for the optical reasons mentioned above.

The test section is approximately 18 inches square. The largest model employed herein is 25 mm in diameter, giving approximately 5% blockage. It is not clear how much extra blockage arises from the cylinder motion. The measured forces are probably slightly high in numerical value due to blockage. The blockage should not be high enough to cause any significant change in flow structure in the near wake.

### 3.5 X-Y towing tank.

The starting cylinder flow investigations were performed in an X-Y towing tank facility. This tank has glass walls on five sides with the top open to the air. The tank is approximately 4.5 meters long with a 1x1 meter cross-section. A computer-controlled carriage rides over the tank providing exact motions both along and across the tank. For this experiment, a one-inch diameter anodized aluminum cylinder was used.

All diagnostics were done using a PIV system. See figure 3.5.1 for a schematic of the optical setup. An argon ion laser was mounted beneath the tank with an inline electro-mechanical shutter and a cylindrical lens. The laser sheet thusly formed was placed in a plane parallel to the floor, emanating from one end of the tank. The camera was mounted to the carriage above the free surface, and a clear Plexiglas plate was used on the free surface to minimize waves and allow for better optical access. To synchronize the motion of the cylinder with the PIV images, an LED was placed in the field of view of the camera and was triggered by a switch that was opened when the carriage moved away from the initial position. Thus the LED dimmed when the carriage began moving. (Since some of the experiments had fairly slow velocity ramps, it was important to have an independent measure of the starting time.) The PIV images were captured to the same type of laser disk recorder used in the oscillating cylinder experiment described in §3.3.

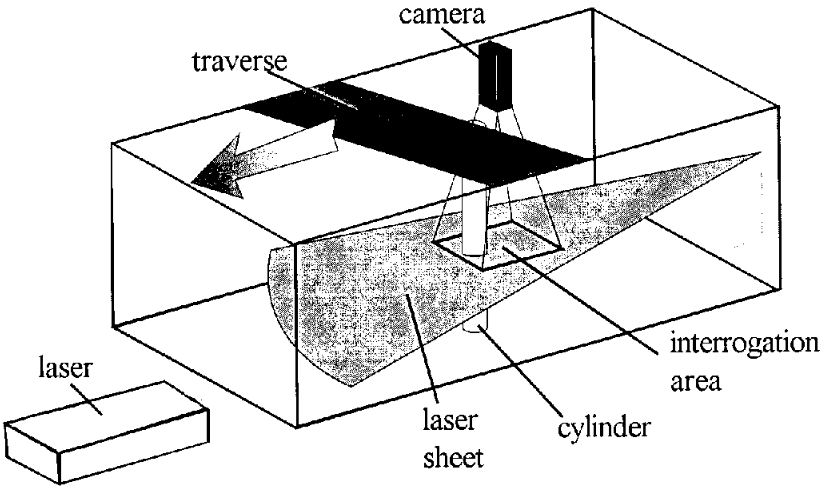

*Figure 3.5.1 - Schematic of the PIV configuration in the X-Y Towing Tank. Camera and cylinder are attached to the traverse. Laser sheet is parallel to the floor, about mid-tank.*

Incidently, the carriage and water tank were identical to the ones used by Williamson & Roshko (1988) in their oscillating cylinder experiment. For the starting flow experiments, the transverse axis, naturally, was not necessary.

# 4

# Starting Cylinder Flow

Before starting the main topic, a moment will be taken to digress to a discussion of earlier work. The rationale will become evident later, although the two topics might seem initially unrelated. This digression concerns a set of experiments on the starting flow around a cylinder. In this experiment, a cylinder, initially at rest, is accelerated at different rates to a constant final speed. For a final Reynolds number above five, the wake forms a stable bubble consisting of two opposite signed vortices. When the Reynolds number exceeds 30-45, the bubble breaks down, oscillates, and then begins vortex shedding. (See Taneda, 1956.) Of particular interest here is the evolution of the forming vortices for Reynolds numbers in the vicinity of 1000.

### 4.1 Evolution of the wake for a cylinder accelerated from rest.

Our interest in the starting flow around a cylinder was to look at the formation process of the wake vortices. Figure 4.1.1 shows a typical sequence in the life of the wake vortices at early time. Plotted are the vorticity fields measured using DPIV. (Vorticity, the curl of velocity, is a convenient measure since it tends to be concentrated in flow structures like vortices, shear layers, and boundary layers.) For this particular case, the cylinder reaches a final Reynolds number of 2000 in 1.6 diameters of forward motion from rest, with the acceleration being constant throughout that time. Note that from rest, the wake is initially symmetrical, consisting of a pair of opposite signed vortices. After some time, this configuration breaks down and one vortex becomes banana shaped. This asymmetrical pattern then breaks down and the wake sheds a vortex.

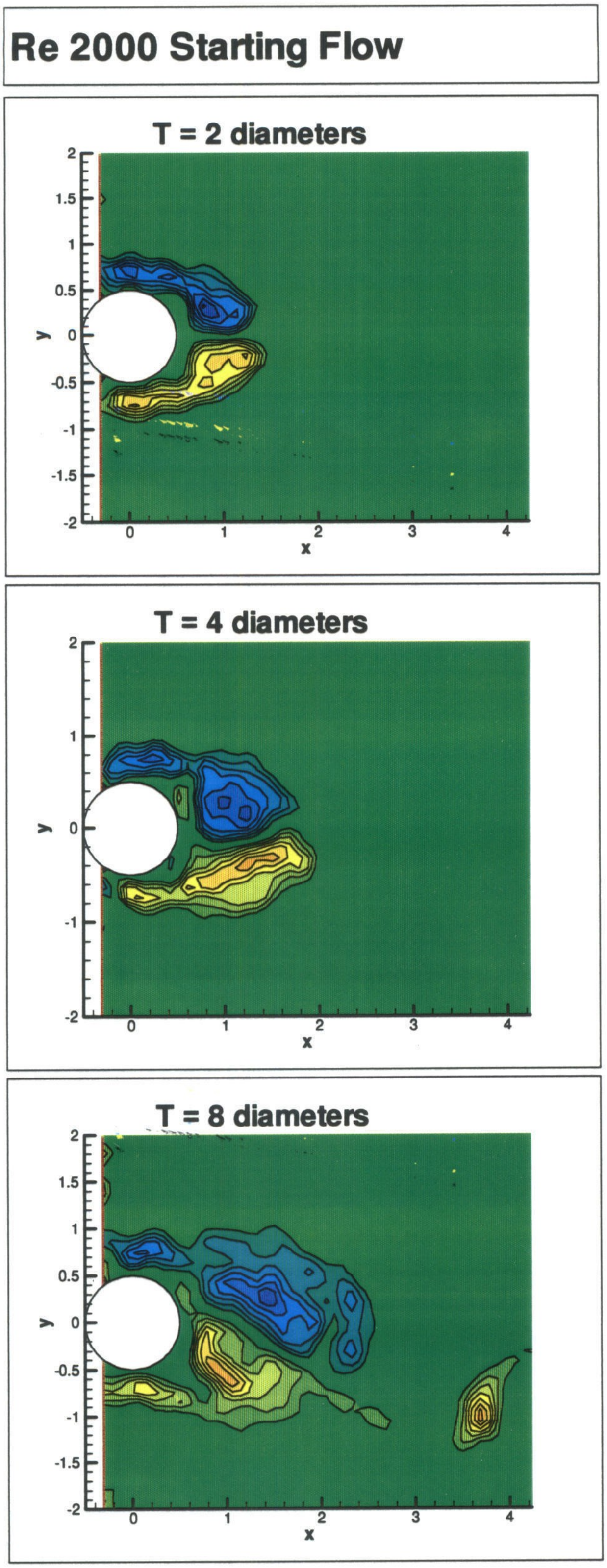

*Figure 4.1.1 - Typical evolution of the wake vortices behind a circular cylinder initially at rest.*

## Empirical mode decomposition in the near wake.

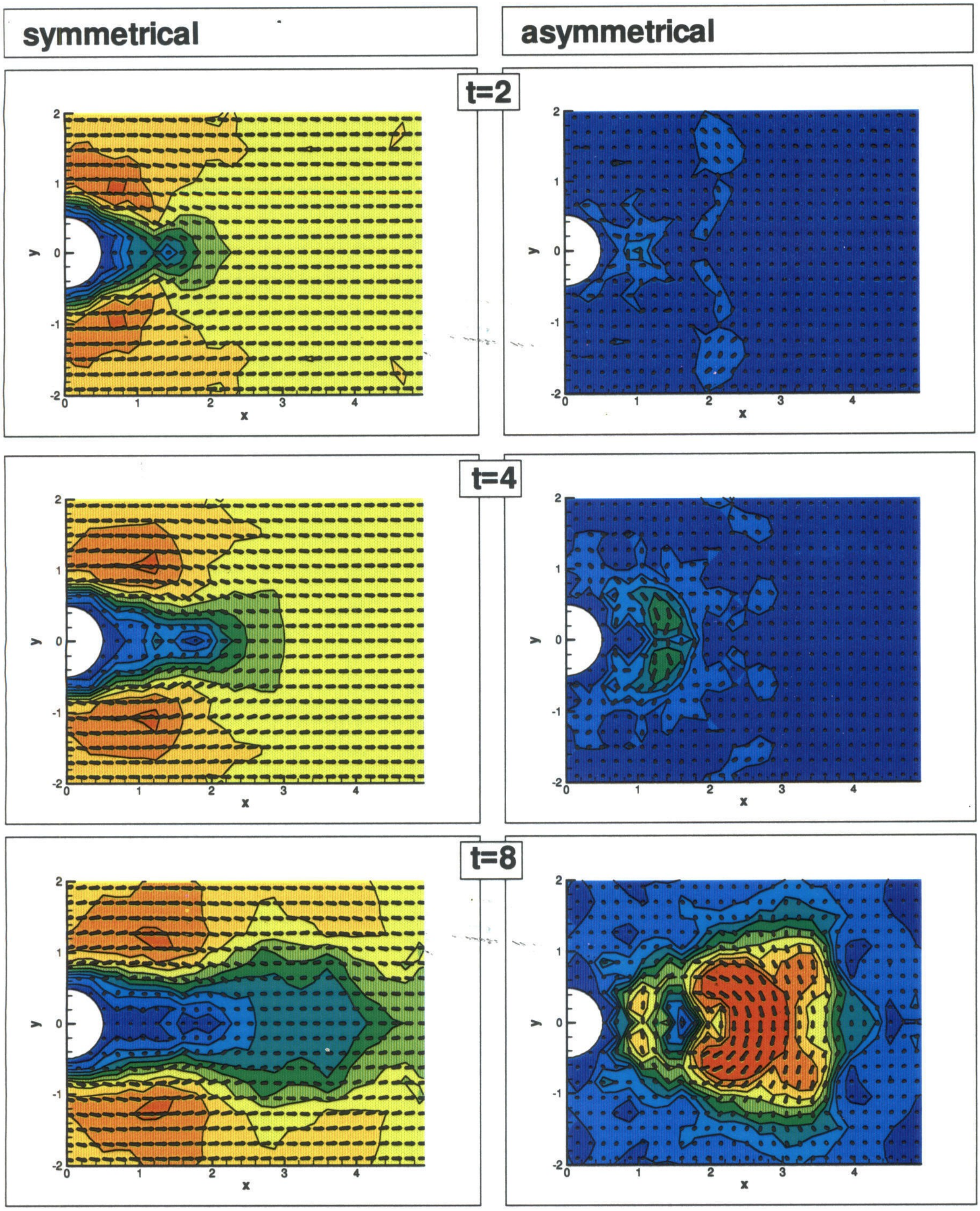

*Figure 4.1.2 - Empirical mode decomposition of the wake of a cylinder initially at rest. The symmetric mode is the mirror symmetric component of the wake. The asymmetrical mode is everything else. Background shading indicates local magnitude of the mode.*

Eventually the wake settles down into the usual Kármán vortex street pattern. Of particular interest is the manner in which this asymmetry manifests itself and leads to shedding.

One way to examine the symmetry breaking process is to directly measure the amount of asymmetry. In private communication with R. D. Henderson, it was suggested that the near wake could be split into symmetrical and anti-symmetrical parts. (At the time, Henderson was using Floquet analysis to determine the critical Reynolds number at which three-dimensionality emerges in the wake. See Barkley & Henderson, 1996.) Strictly speaking, one would have to find and measure the first eigenmode with a significant asymmetrical component, something which is beyond the scope of this work. As a good approximation to this, the near wake was divided into two parts, one which was mirror symmetric (streamwise velocity equal, transverse velocity opposite), and one which was everything else (anti-symmetrical part). To measure the amount of asymmetry, norms based on the integral value of the magnitude of the asymmetrical part were taken. For example, the infinity norm of the asymmetry would be the largest asymmetrical velocity magnitude in the

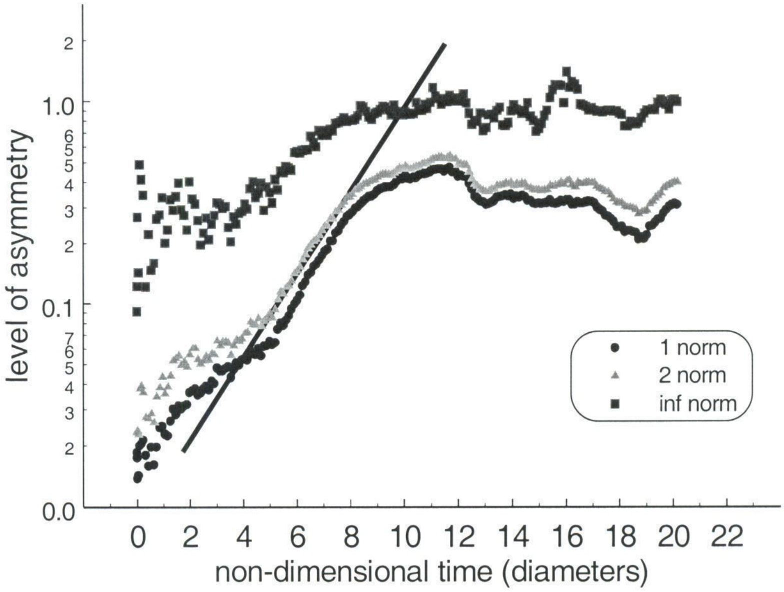

*Figure 4.1.3 - Comparison of the various norms of the asymmetrical mode of the near wake. Straight line to indicate the region of nearly exponential growth.*

near wake and the one norm would be the sum of the magnitudes in the same region. Figure 4.1.2 shows an example of what these velocity fields look like. As expected, the symmetrical part looks like the original vortex pair at very early times. Interestingly, the asymmetrical part looks like a large vortex sitting in the middle of the near wake. A comparison of the various norms is shown in figure 4.1.3. The asymmetry grows exponentially (a straight line on this semi-log plot) from the noise floor before reaching some kind of saturation. The exponential growth of the instability would suggest that the near wake is linearly unstable, although it is unknown from this plot whether the wake becomes unstable after starting stable or if this measurement is simply noise limited by the inability to measure the very low velocities present at early times.

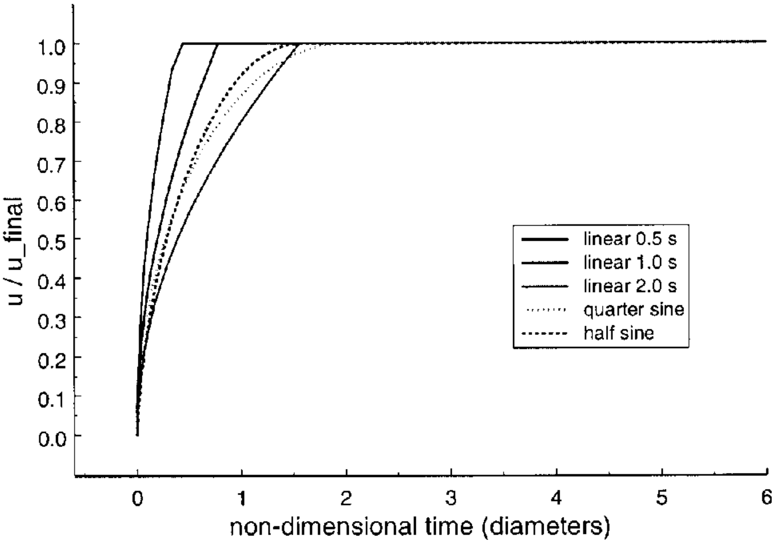

*Figure 4.2.1 - Velocity ramps used for the starting flow experiments.*

### 4.2 Evolution of the circulation of the wake vortices.

As mentioned in §2.2, a look at vortex ring formation helps to clarify this formation process. Gharib, et al. noticed that when vortex rings are generated, there is a limit to the amount of circulation that can be packed into the ring itself. After this level is reached, the ring begins to move off and the rest of the circulation ends up in a trailing jet-like structure. Moreover, this level of circulation was consistently reached at

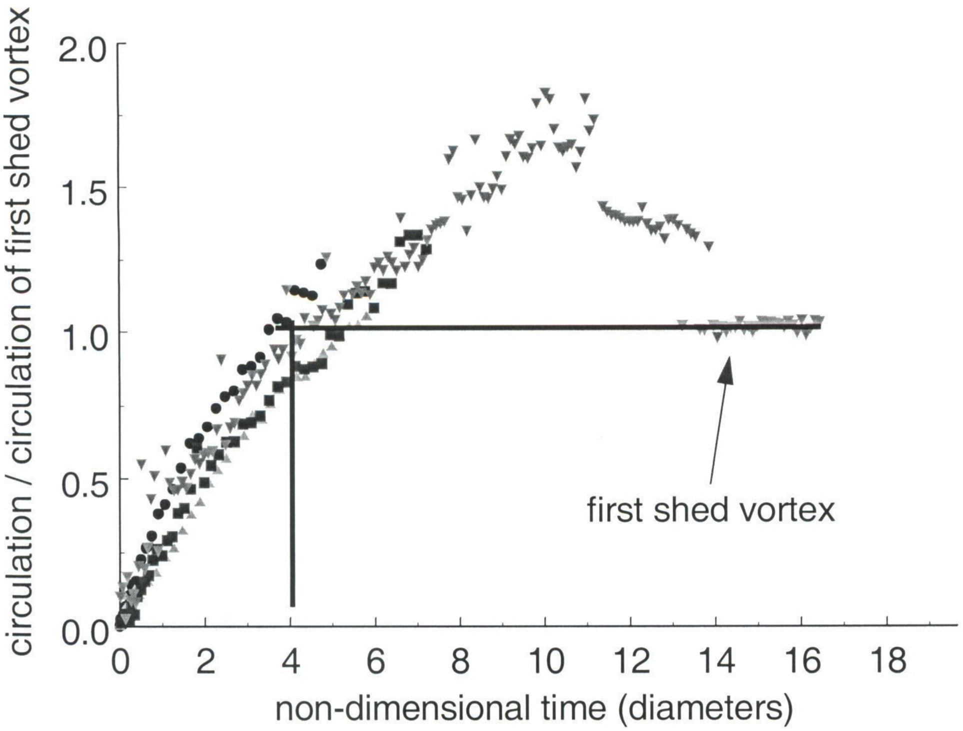

*Figure 4.2.2 - Circulation of the starting vortex scaled by the first shed vortex as a function of non-dimensional time (distance travelled in diameters).*

a non-dimensional time of four diameters, where time is scaled by the average velocity and the diameter of the generating piston. Since time*average velocity is the same as the distance travelled, this is equivalent to the stroke ratio (length of stroke divided by the diameter of the generator). Vortex rings of stroke ratios below four would form as clean rings with circulation rising as the stroke ratio increased towards four. After four, the rings are trailed by a large jet-like structure containing whatever circulation was generated after time four. Analogous experiments were performed for the starting cylinder.

As mentioned above, the time scale is based on the average velocity. For the cylinder, this measures the number of diameters of motion from rest.

$$t^* = \frac{t\bar{U}}{D} = \frac{t}{D}\frac{1}{t}\int_{t_0}^{t} U\,dt' = \frac{S}{D} \qquad \text{(eq 4.2.1)}$$

Average velocity is chosen to greatly reduce the dependency on the acceleration profile. Since no experimental apparatus can generate truly impulsive starts, this formulation allows us to start the cylinder more gradually without losing the ability to compare different cases. Examples of the different velocity ramp profiles is shown in figure 4.2.1.

Results of several runs are plotted in figure 4.2.2. Shown are circulation values (scaled by the first shed vortex's circulation) vs time. Care was taken to avoid including the secondary vortices on the rear surface of the cylinder when the circulation was computed. Although there is some amount of variability, the formation time is again clustered around *four diameters. Once again, this points to some kind of event happening* around t*=4.

### 4.3 Deviation from normal evolution at low acceleration.

An interesting side note is the effect of low acceleration on flow evolution. Plotted in figure 4.3.1 is a comparison of two cases, identical except for ramp profiles. Both cases, in fact, accelerate to the same final Reynolds number in the same amount of dimensional time. However, the deviation from normal evolution (see §4.1) is rather clear: the wake appears to shed quasi-symmetrically at lower acceleration. So the significant event occurring at t*=4 apparently needs a sufficiently vigorous starting process to begin.

The exact level appears to be a function of experimental conditions. Sarpkaya (1991) uses a quick-acting valve to start the water flow for final Reynolds numbers between 16,000 and 50,000; this transition happens at much lower accelerations than for these towing tank experiments.

**Effect of acceleration on formation process.**

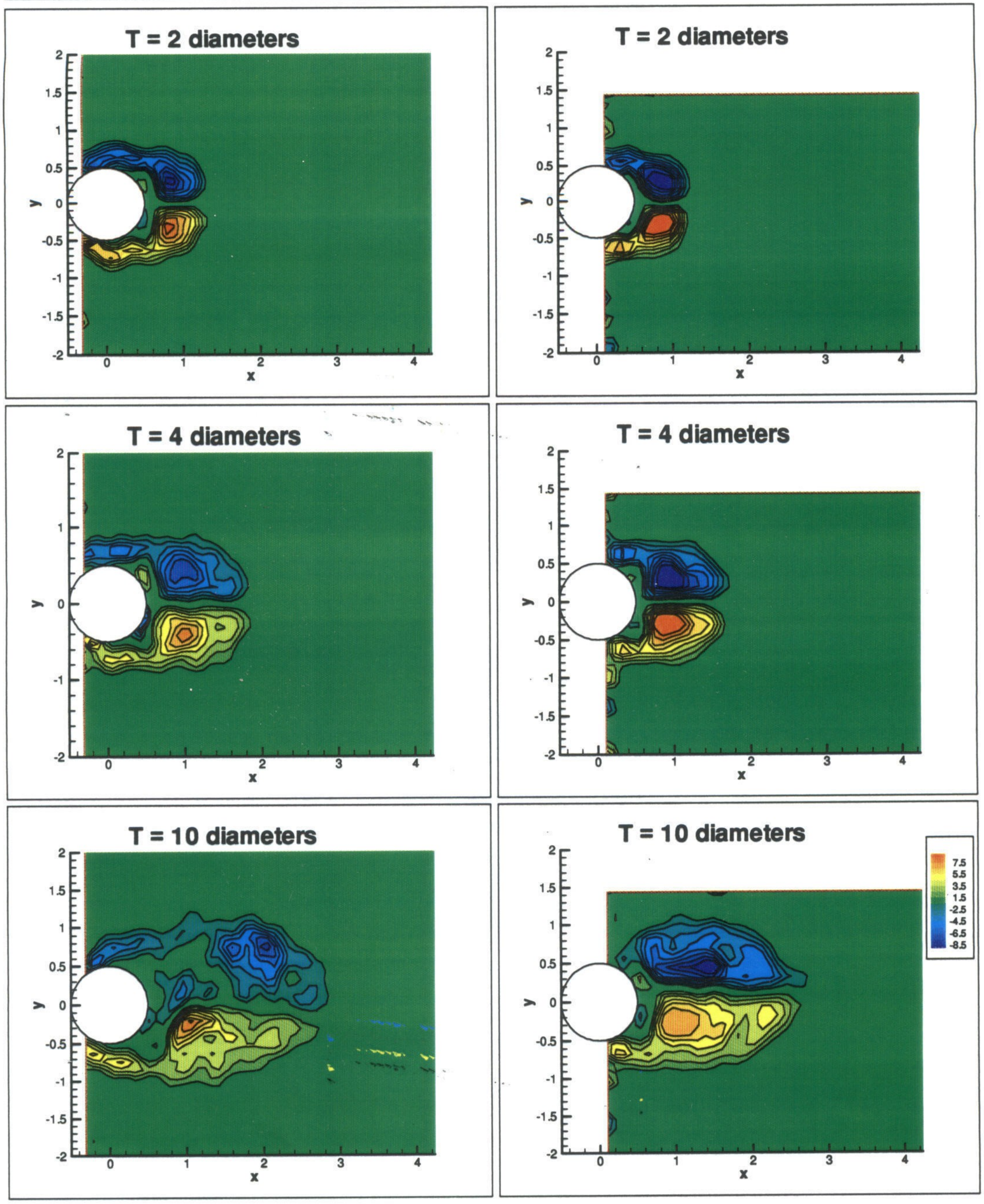

*Figure 4.3.1 - Comparison of two starting flow cases, differing only in acceleration profile. Note how the lower acceleration case (on the right) is nearly symmetrical at time = 10 diameters, when the higher acceleration case is about to shed.*

Likewise, for computational studies, where the background noise comes primarily from round-off and discretization error, the wake is stable to even higher acceleration. (Frequently a perturbation has to be introduced into the computation to initiate the symmetry breaking.)

### 4.4 Explanation of the drag overshoot.

While searching for the underlying cause of the transition at t*=4, the so-called drag overshoot problem described in Sarpkaya's paper proved interesting. As shown in figure 4.4.1, for normal acceleration, there is a curious peak in the drag before it settles down. The spike happens at t*=2, and a rather uninteresting event happens at t*=4. To explain this behavior, a simple model was developed for the initial drag behind the cylinder.

Using the impulse formulation for force (Saffman, 1992),

$$\text{force} = \frac{d}{dt}\left(\rho\int \mathbf{x}\times\varpi dV\right) \rightarrow \frac{d}{dt}\int \rho\mathbf{u}dV \qquad \text{(eq 4.4.1)}$$

one can approximate the forces on the cylinder by modelling the wake as a pair of point vortices. Substituting in the point vortex vorticity field and taking the force component in the drag direction, one gets

$$\text{drag} \approx \frac{d}{dt}(y\Gamma) \qquad \text{(eq 4.4.3)}$$

since the vorticity field reduces to a pair of delta functions. Expanding this relationship, this becomes

$$\text{drag} \approx y\frac{d\Gamma}{dt} + \Gamma\frac{dy}{dt} \qquad \text{(eq 4.4.4)}$$

Although the vortices move towards the back at the earliest time, by the time the drag overshoot becomes important, the vortices are nearly stationary, only growing steadily in circulation. Hence the second term on equation 4.4.4 would be negligible. So it would seem, in this model, the

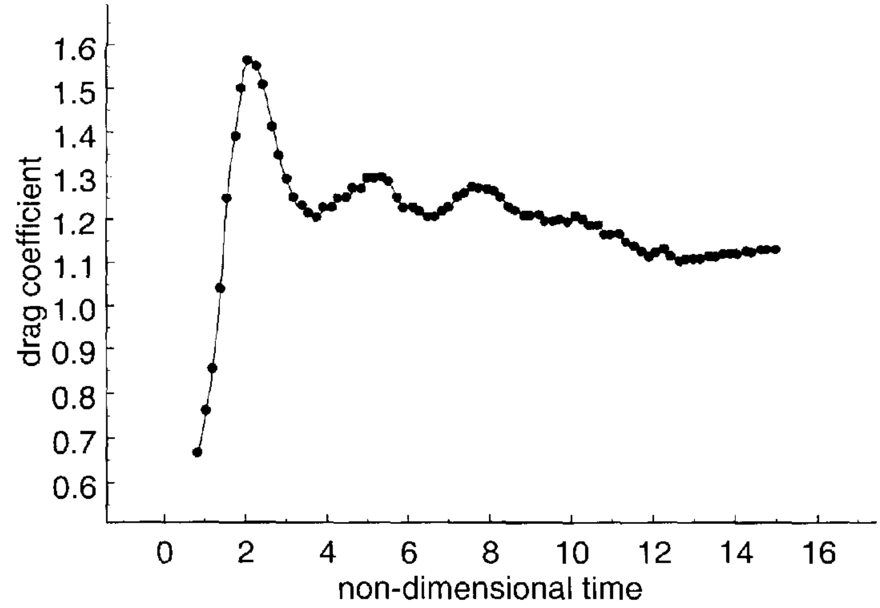

*Figure 4.4.1 - Drag coefficient for a starting cylinder at early time. Note the large peak around t*=2 diameters. From Sarpkaya (1991).*

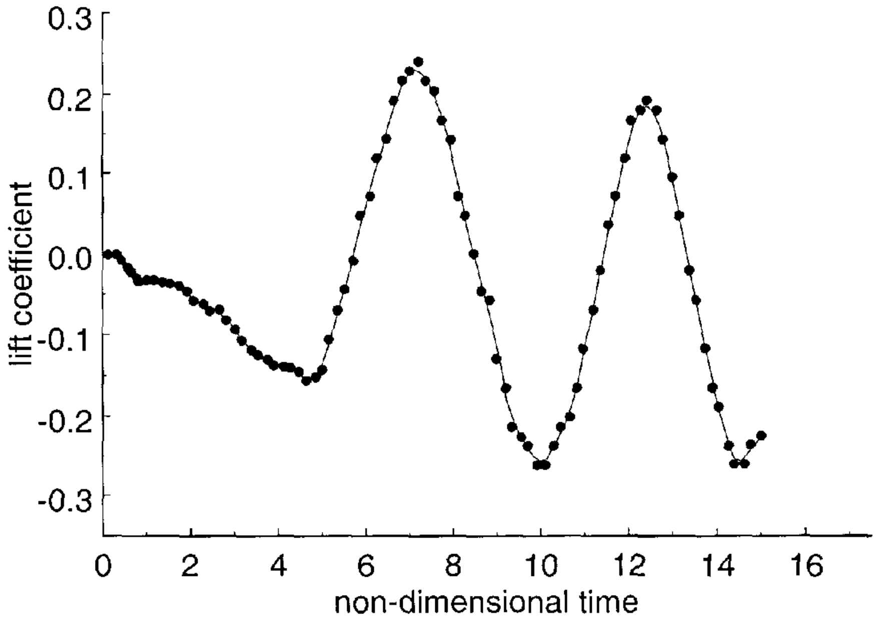

*Figure 4.4.2 - Lift coefficient for a starting cylinder at early time. Note the change in lift behavior at t*=4. From Sarpkaya (1991).*

drag at early time is related to the rate of change of the circulation of the wake vortices. Let us therefore look at the terms which contribute to circulation flux. From Morton (1984), for a rigid body moving through a single density fluid, there are three terms of interest: pressure gradients along the body, tangential acceleration of the body, and vorticity annihilation. Neglecting viscous effects, the circulation in the wake vortices should go as

$$\frac{d\Gamma}{dt} \approx \frac{dP}{ds} + \frac{dU_{body}}{dt} + \text{annihilation} \qquad \text{(eq 4.4.5)}$$

Since the cylinder has generally reached equilibrium speed by this point, the pressure gradient term is likely constant and the body acceleration term is zero. Hence the drag overshoot phenomena looks to be linked to vorticity annihilation in the wake. It would therefore appear that what happens in the wake is that at t*=2, the wake vortices first "feel" the presence of each other in the form of annihilation. Therefore, the steadily rising drag takes a sudden dive at that point. Then at t*=4,

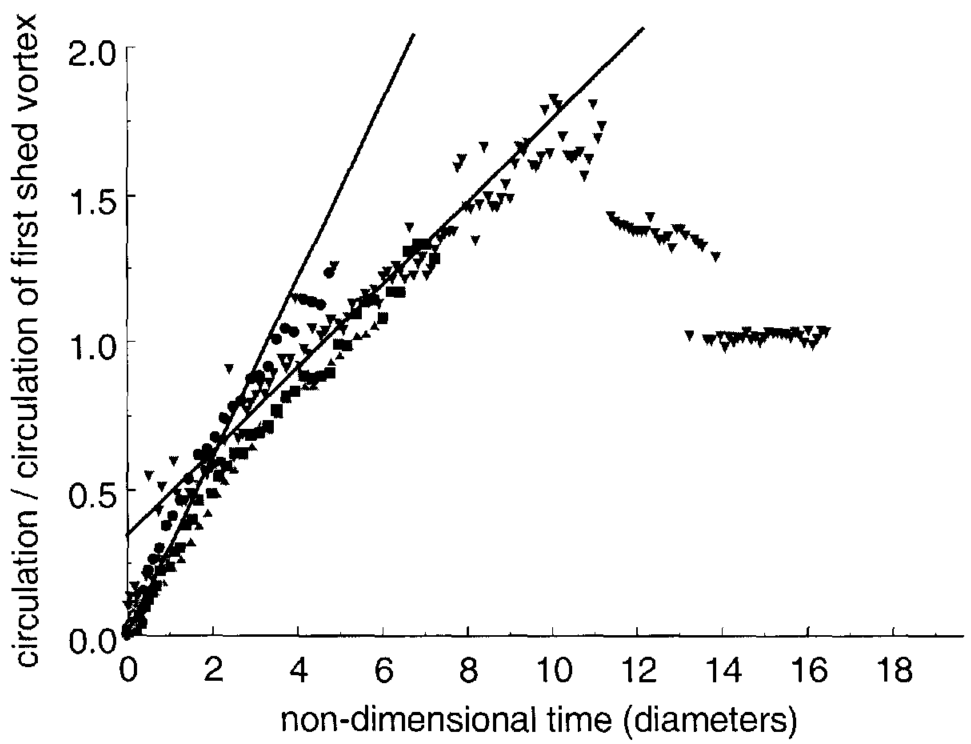

*Figure 4.4.3 - Circulation as a function of time with lines to indicate the two different circulation growth rates at earlier and later times.*

the annihilation appears to reach a critical point, as the variation in drag rapidly levels off. Coincident with this change is a sudden change in lift as seen in figure 4.4.2. Of course, if this were the case, there should be a change in the slope in the circulation plot (figure 4.2.2). Figure 4.4.3 shows the slope change on the data in figure 4.2.2. The circulation growth rate clearly decreases around $t^*=2^+$ to a lower value. From figure 4.2.1, this drop is not due to acceleration ending (since the ramps end before $t^*=1.5$). To make sure that the decreased growth rate was not due to a feedback mechanism cutting off the supply of vorticity from the cylinder, the circulation flux into the vortices was measured by integrating the flux of vorticity flowing through the separated shear layers at three stations. From figure 4.4.4, it seems that the circulation flux from the cylinder is essentially constant. Hence the drop in circulation growth of vortex is not due to a decrease in input flux, but to an increase in vorticity loss. Since the main vortices are advected into each other

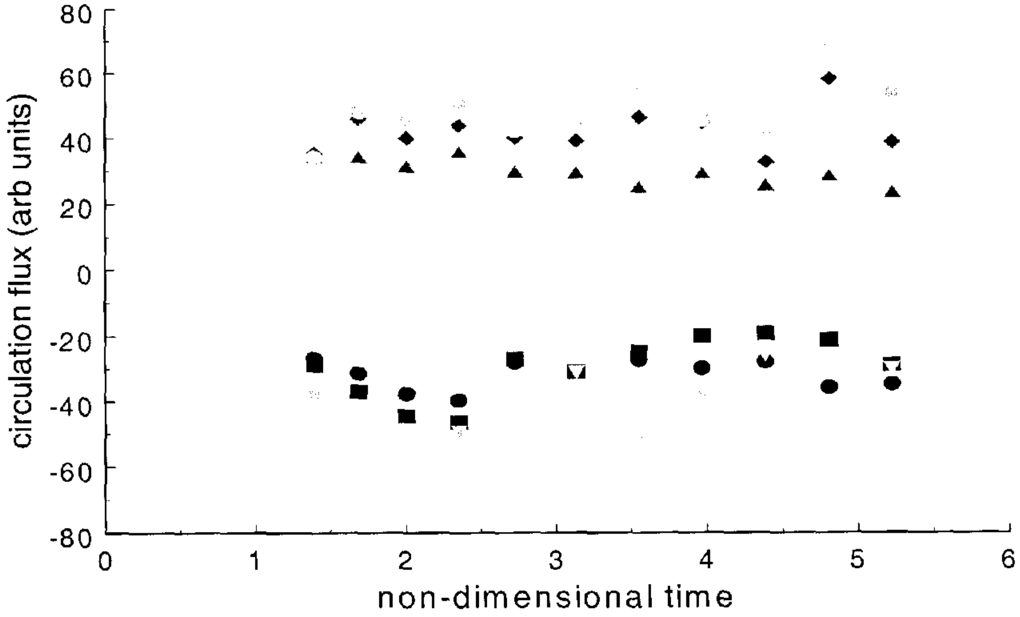

*Figure 4.4.4 - Circulation flux through the separated shear layers feeding the main vortices in the wake of the starting cylinder. The decrease in flux appears to much less than the decrease in circulation growth rate observed in the vortices.*

around $2 < t^* < 4$, the vorticity annihilation rate should rise dramatically around this time. In addition, the wake stagnation point – where the streamlines from the two separating shear layers meet – effectively shuts out ambient fluid from the wake. This greatly reduces entrainment into the wake, which keeps the fluids velocities low in the region behind the cylinder. Consequently, the dominant mechanism for loss of circulation flux comes from advection-driven vorticity annihilation in the wake where the two main vortices are pressed into each by the high freestream pressure.

Combined with the previous results concerning asymmetry and critical circulation, this would imply that the wake reaches a critical condition around $t^*=4$. At this point, the two main vortices in the wake begin to interact with each other, leading to vorticity annihilation. The wake begins to become strongly asymmetrical, hits a critical level of circulation, and reaches a saturation level of vorticity annihilation. (As long as the Reynolds number and acceleration are high enough to trigger the instability, of course.) Consequently, the wake transitions from the symmetrical vortex pair to the asymmetrical pair with the banana shaped vortex, and the forces show a leveling off of the drag and a transition in the lift.

# 5

# Oscillating Cylinder Flows

This study is focused on the interaction between the vortices in the near wake as a function of the cylinder motion. From earlier work (see Bishop & Hassan, 1964 and Williamson & Roshko, 1988), it is known that there is some kind of synchronization of the near wake to the motion when the motion frequency is near the frequency of the wake of the stationary cylinder. Of particular interest is the manner in which the wake (and hence the forces) have been seen to change phase on either side of a critical frequency. Consequently, this chapter begins with an overview of the various observed phenomena, both in terms of forces and vortex dynamics in the near wake. This includes an examination of the effects of adding streamwise motion. Then the notion of formation time as it relates to the oscillating cylinder is explored and connected to the phase shifting phenomena. Finally, the “2P” mode in the wake will be revisited, and a plausible explanation for the source of this wake behavior will be proffered.

### 5.1 Evolution of the wake.

The most direct way to examine wake behavior is to study the vorticity in the wake. This is especially true for bluff body wakes (like cylinders) that are dominated by the presence of large vortices. For forced motion experiments, it is natural to phase average the results since the phase relationship is known. For self consistency every run is phase averaged by the transverse position. Not only does this reduce the residual noise in the vorticity plots, it also simplifies comparison across different motions since they all have a common reference. Figures 5.1.1-

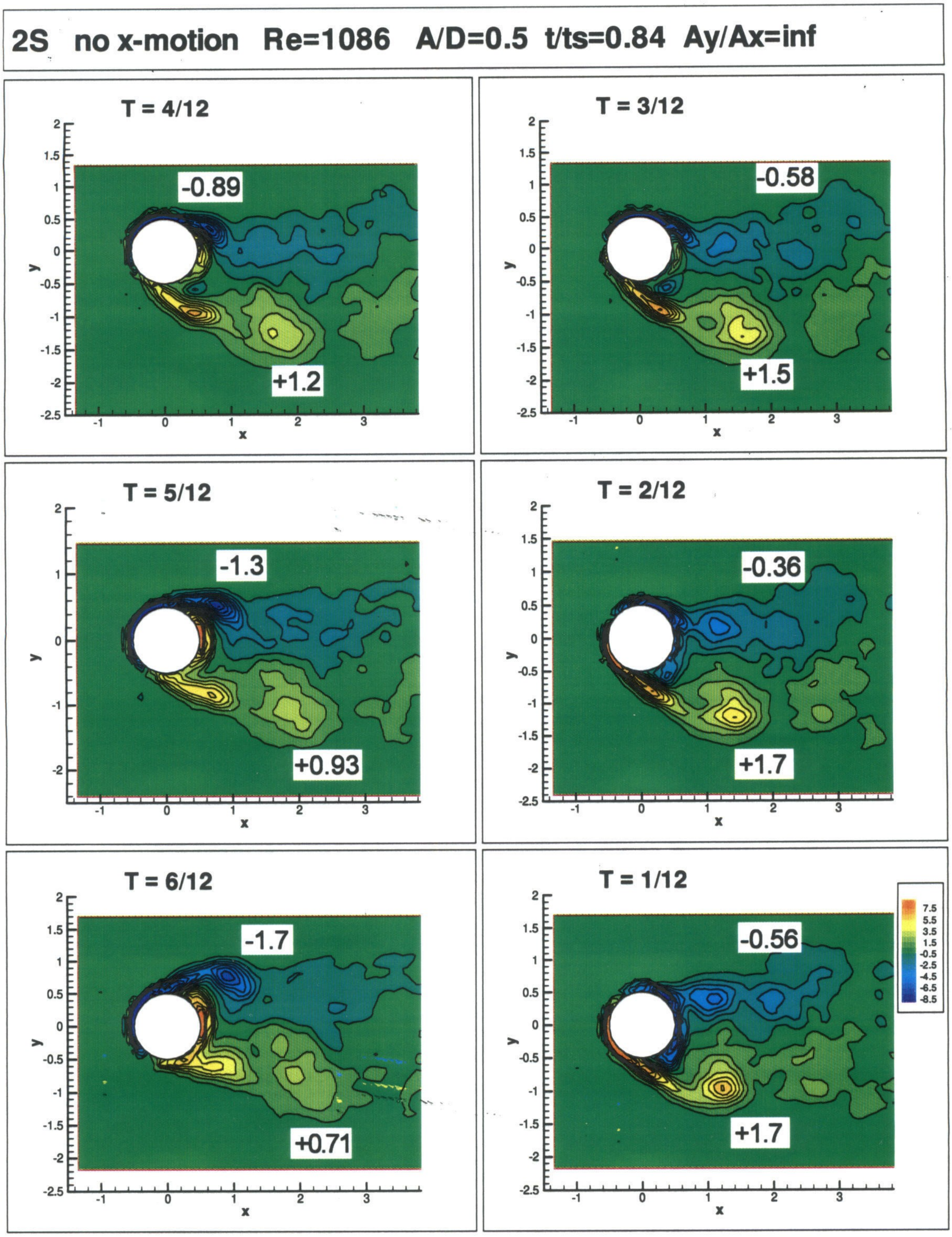

*Figure 5.1.1 - Phase averaged vorticity for nominal 2S case with no streamwise motion. Upper half cycle of motion. Numbers indicate circulation of vortex.*

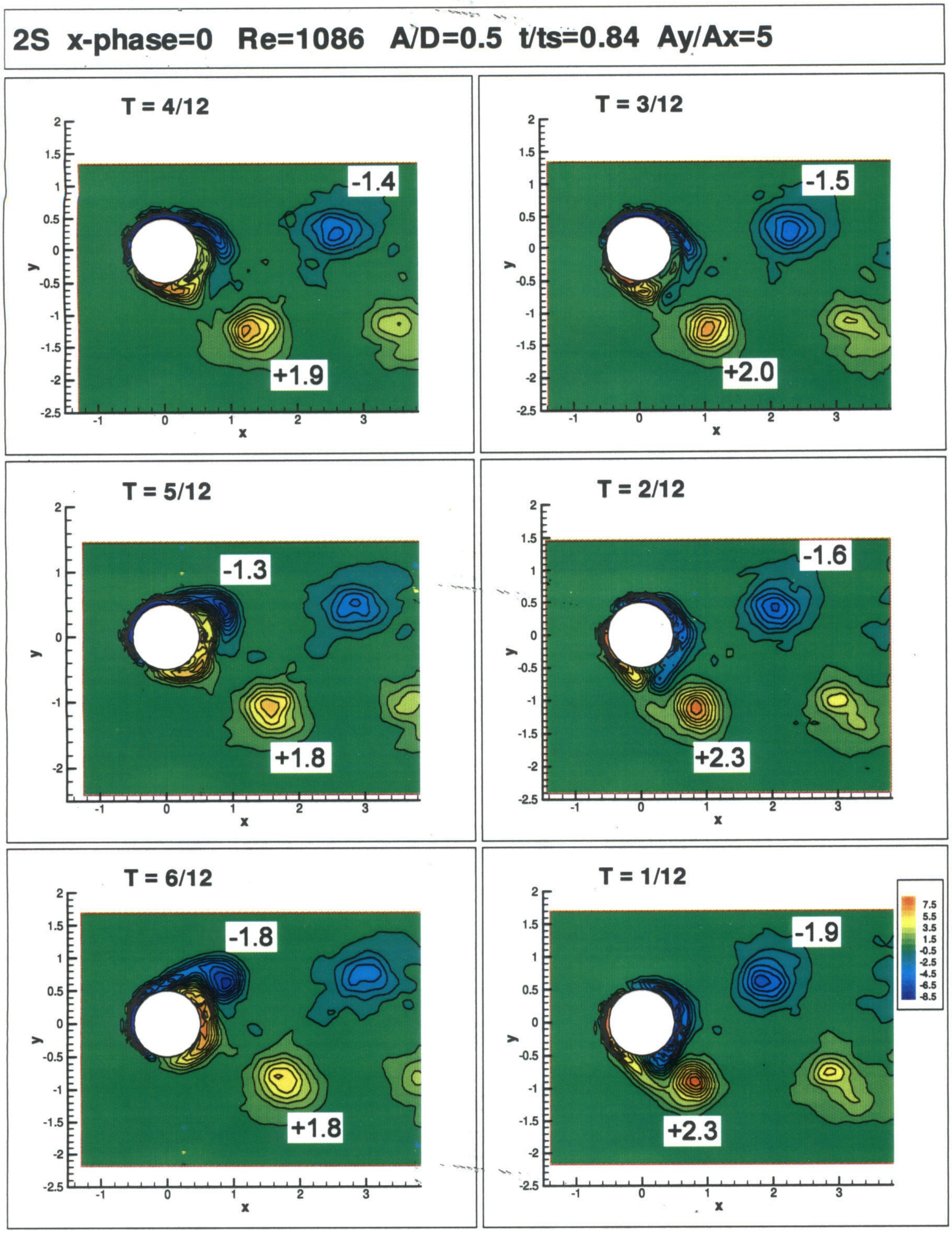

*Figure 5.1.2 - Phase averaged vorticity for transverse motion in the 2S region with streamwise motion at 0 degrees phase. Upper half cycle of motion. Numbers indicate circulation of vortex.*

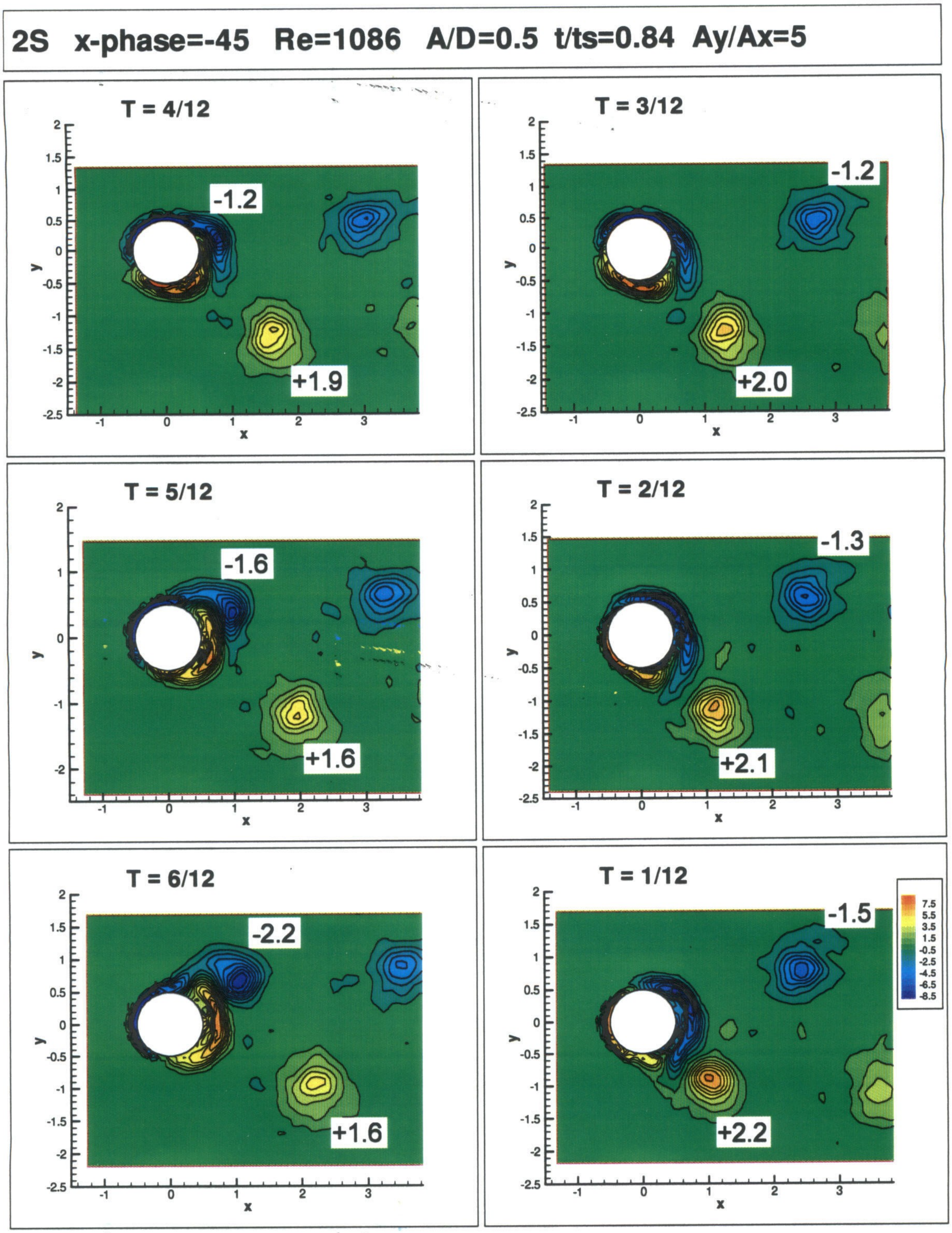

*Figure 5.1.3 - Phase averaged vorticity for transverse motion in the 2S region with streamwise motion at -45 degrees phase. Upper half cycle of motion. Numbers indicate circulation of vortex.*

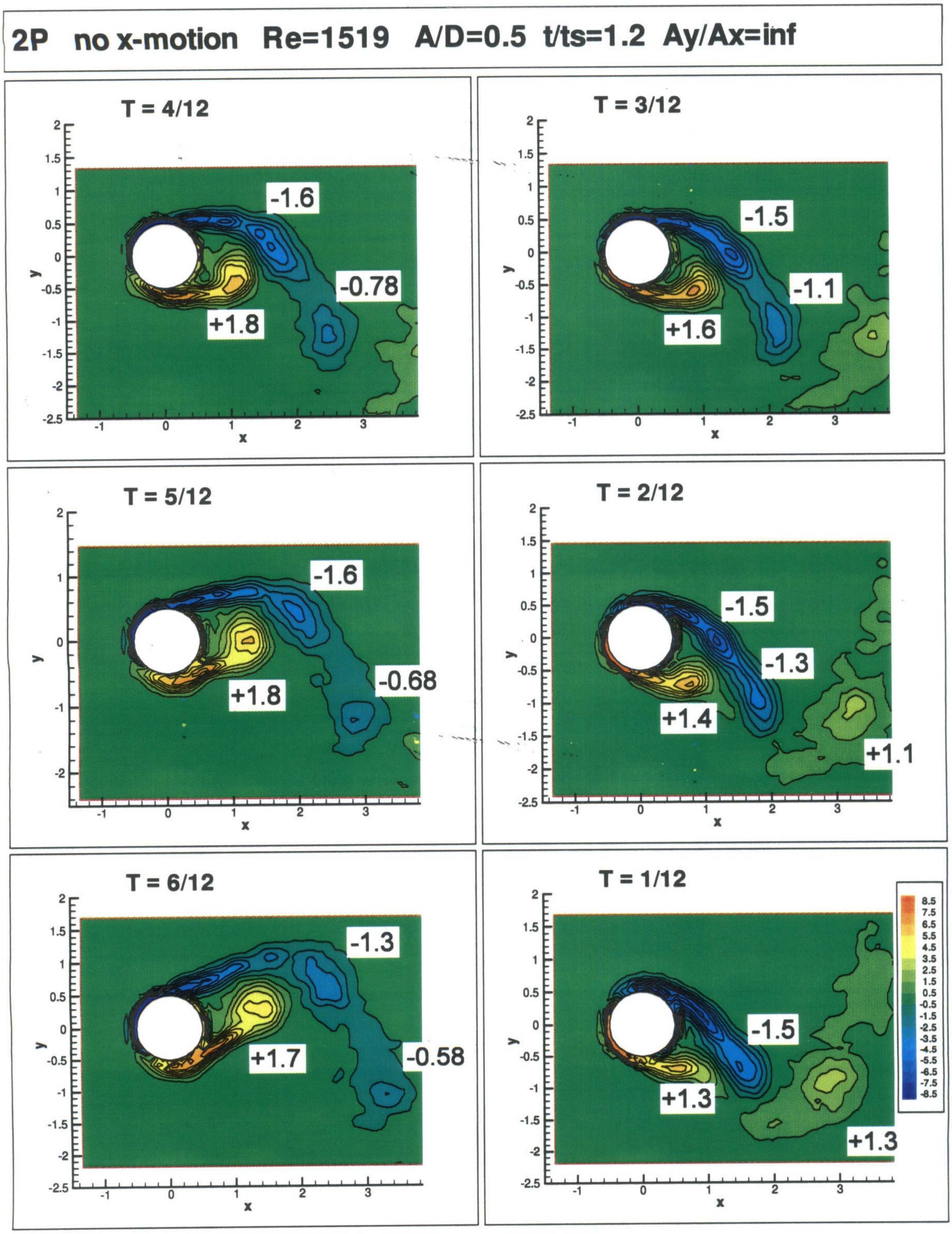

*Figure 5.1.4 - Phase averaged vorticity for nominal 2P case with no streamwise motion. Upper half cycle of motion. Numbers indicate circulation of vortex.*

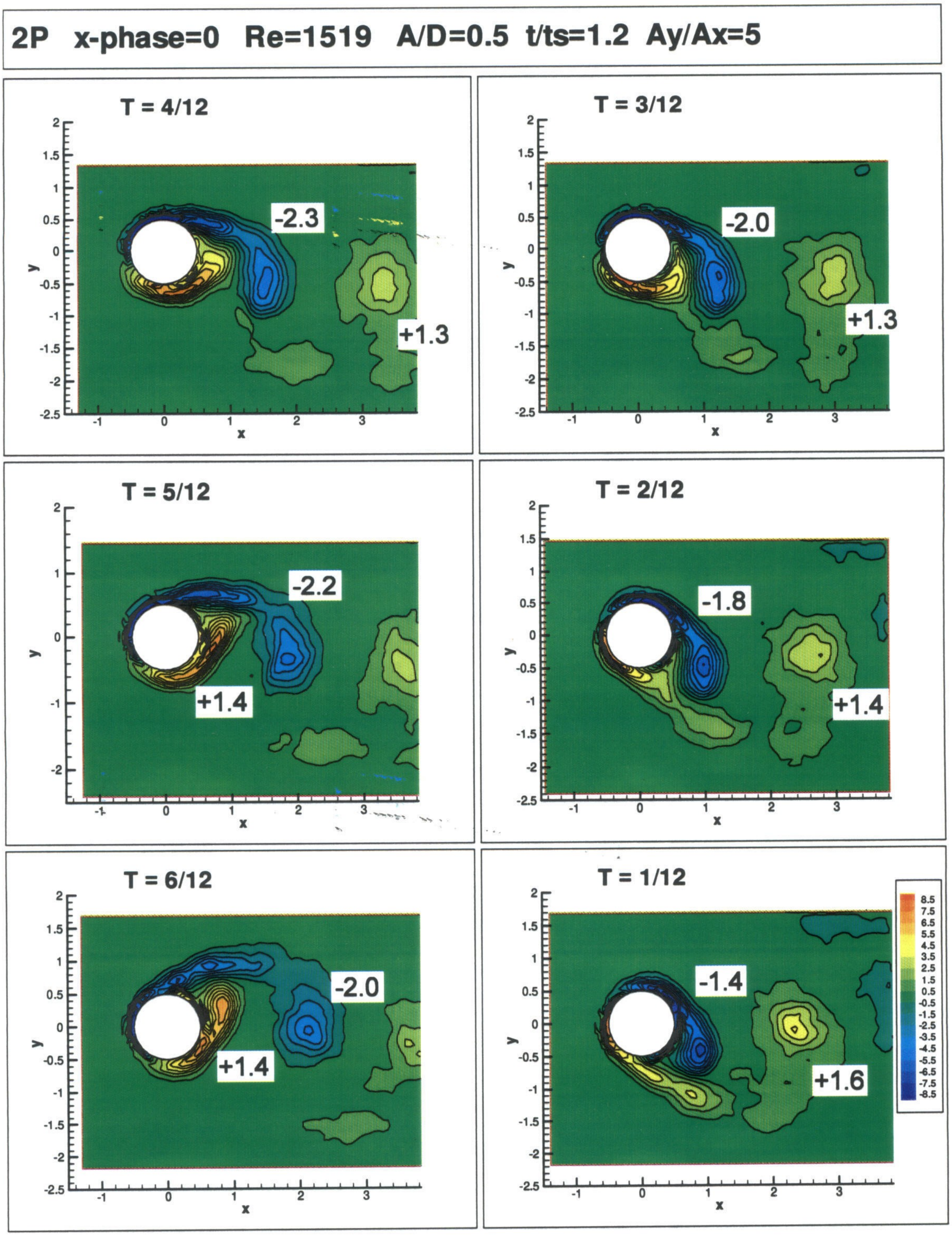

*Figure 5.1.5 - Phase averaged vorticity for transverse motion in the 2P region with streamwise motion at 0 degrees phase. Upper half cycle of motion. Numbers indicate circulation of vortex.*

**2P x-phase=-45 Re=1519 A/D=0.5 t/ts=1.2 Ay/Ax=5**

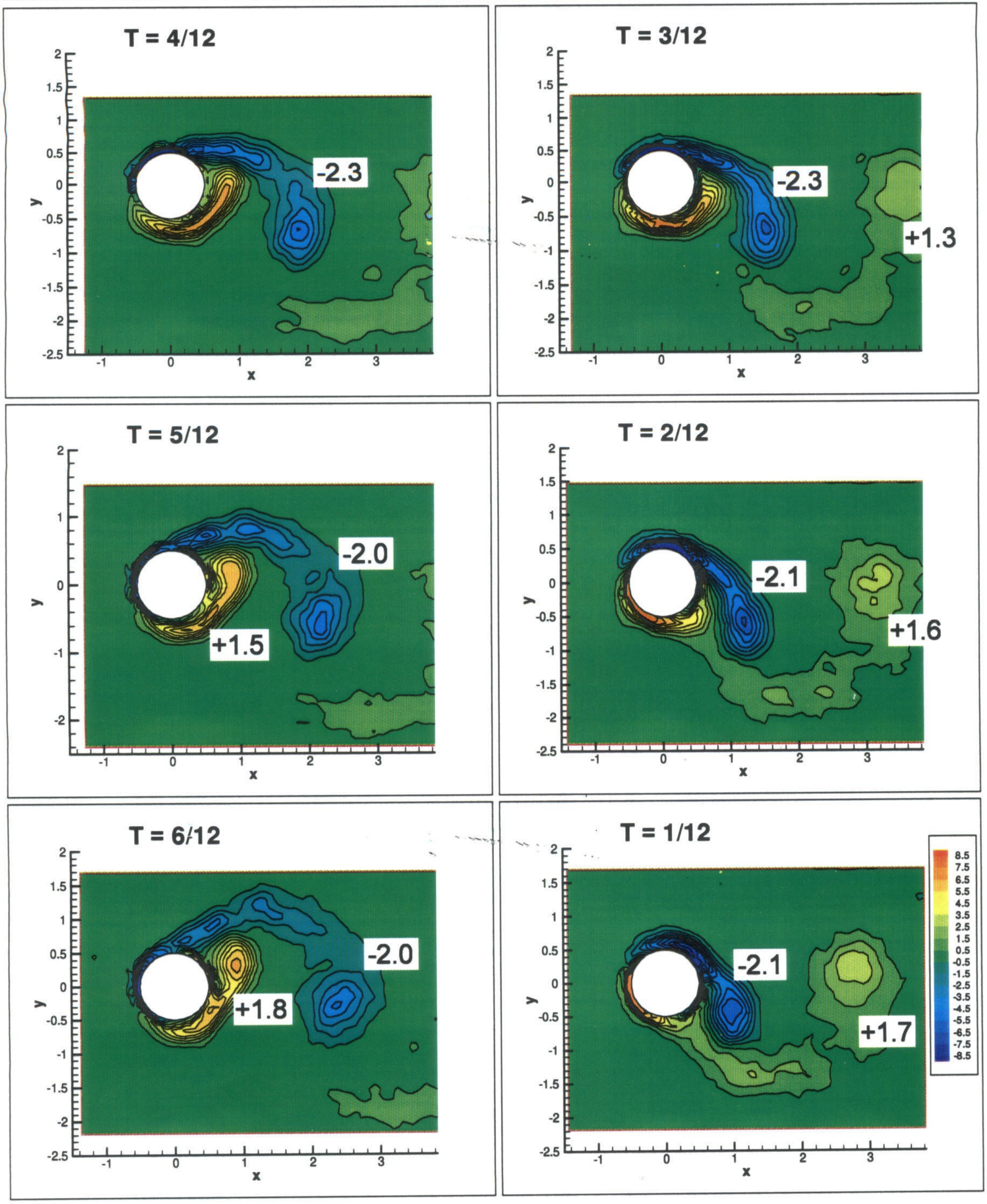

*Figure 5.1.6 - Phase averaged vorticity for 2P case with streamwise motion at -45 degrees phase. Upper half cycle of motion. Numbers indicate circulation of vortex.*

5.1.6 show phase averaged vorticity for six typical parameters. Since the associated velocity fields have all been non-dimensionalized, the figures are showing non-dimensionalized vorticity ($\omega D/U_\infty$). The first three are with the transverse motion in the nominal 2S range and the latter three in the nominal 2P range. Within each set of three, the effects of both streamwise motion and streamwise phase are shown. The first of each three has no streamwise motion (1-DoF), the second with streamwise motion at 0°, and the third with streamwise motion at -45°. The plots show the cylinder in six phases of motion in the upper half of the cycle. Vortices are labeled with their non-dimensional circulation, calculated by taking the area integral of vorticity in the vortex. The relative positions of the phases are illustrated in figure 5.1.7.

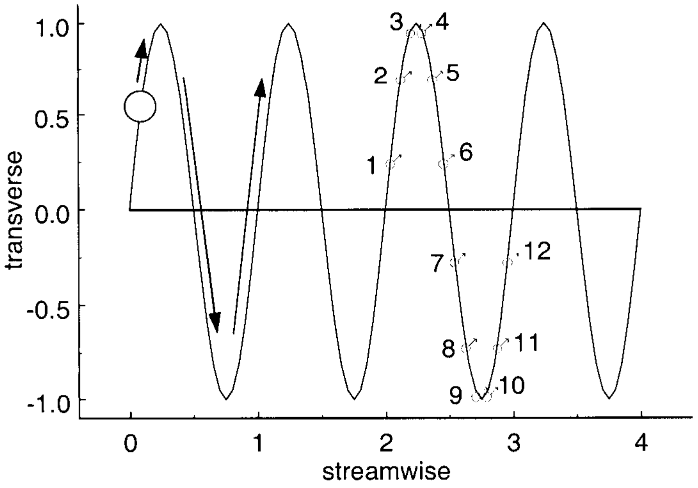

*Figure 5.1.7 - Position of the cylinder for the phase averaged plots. Phases are equidistant in time.*

First of all, the 2S and 2P modes are apparent in the vortex patterns; this implies that the right parameter regions have been found. (The parameters were selected by changing freestream speed while maintaining the same motion amplitude and frequency. This varies the Strouhal frequency, which in turn switches the wake from the 2S to the 2P mode.) Note in figure 5.1.4 the presence of the vortex pairs, a structure that is clearly not present in the 2S region. It is also apparent that the wake is much longer in the 2P region, especially in the 1-DoF cases.

## Comparison at time 3/12.

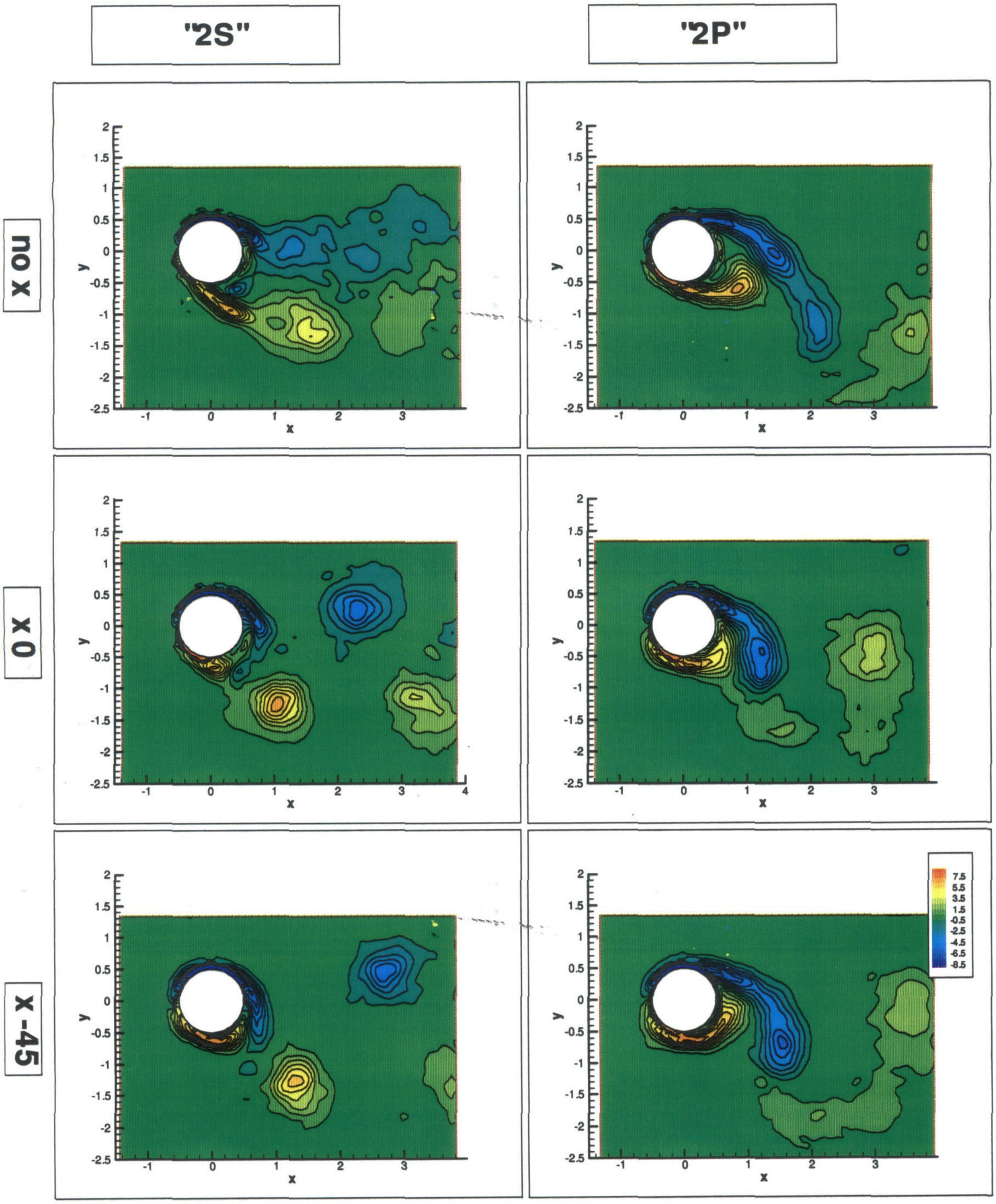

*Figure 5.1.8 - Comparison of different parameters at a constant transverse phase. Each case is shown when the cylinder is nearly at the upper extrema of motion. Note the dramatic change in wake behavior when the streamwise motion is added.*

The effect of adding the second DoF is also quite apparent. This is emphasized in figure 5.1.8, where the different cases are presented together for ease of comparison. Note in the 2S case the rather remarkable increase in phase coherence once the streamwise motions are added. In the 2P case, the second DoF causes the characteristic large dead-water region to disappear – along with the pairing behavior. The phase of the streamwise motion is also apparent in the way it can shift the wake. Notice how the wake can be displaced by about one cylinder diameter by shifting the phase 45°. (Compare the positions of the vortices in the bottom two rows of figure 5.1.8.) This figure also more clearly demonstrates the apparent phase flipping in the wake: the figures on the 2S column appear to be about to shed from the lower side, while the opposite is true on the 2P column. (Note: "2S" and "2P" are used to describe the transverse motion, and not the number of vortices shed.)

Consequently, it would appear that the primary effect of adding a small amount of streamwise motion (about 0.1 diameters) is to control the phase of shedding. Figure 5.1.9 gives an indication of how small the

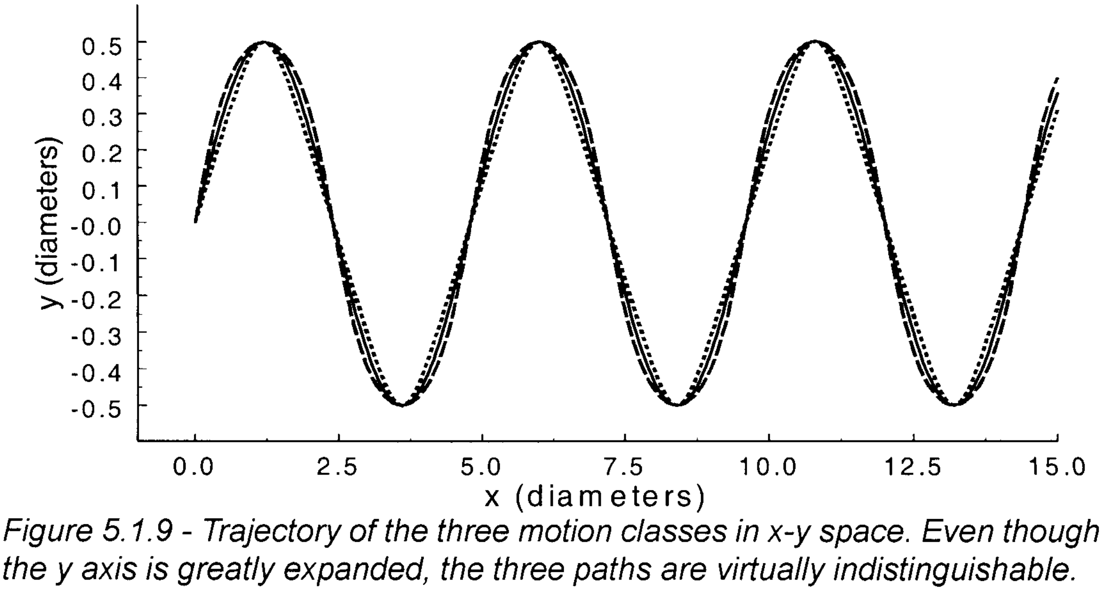

*Figure 5.1.9 - Trajectory of the three motion classes in x-y space. Even though the y axis is greatly expanded, the three paths are virtually indistinguishable.*

streamwise perturbation is. There appears to be no change in the shedding frequency (since the wake is still phase locked to the transverse frequency). Two phase-related effects are readily evident: the increased phase coherence and the ability to shift the wake in phase. It would seem that the transverse motion sets the overall rate of shedding while the streamwise motion can alter the relative timing. Presumably the regular injection of circulation via acceleration of the body helps to stabilize the phase of the wake. By better coordinating the phase of shedding, one would automatically get increased phase coherence; hence, the shedding would happen at a more regular time within the cycle. Furthermore, it would appear that even this small amount of streamwise motion is enough to affect a fairly large scale shift in the wake. Displacing the vortices on the order of a diameter is quite significant when the distance traveled per cycle is only on the order of five diameters.

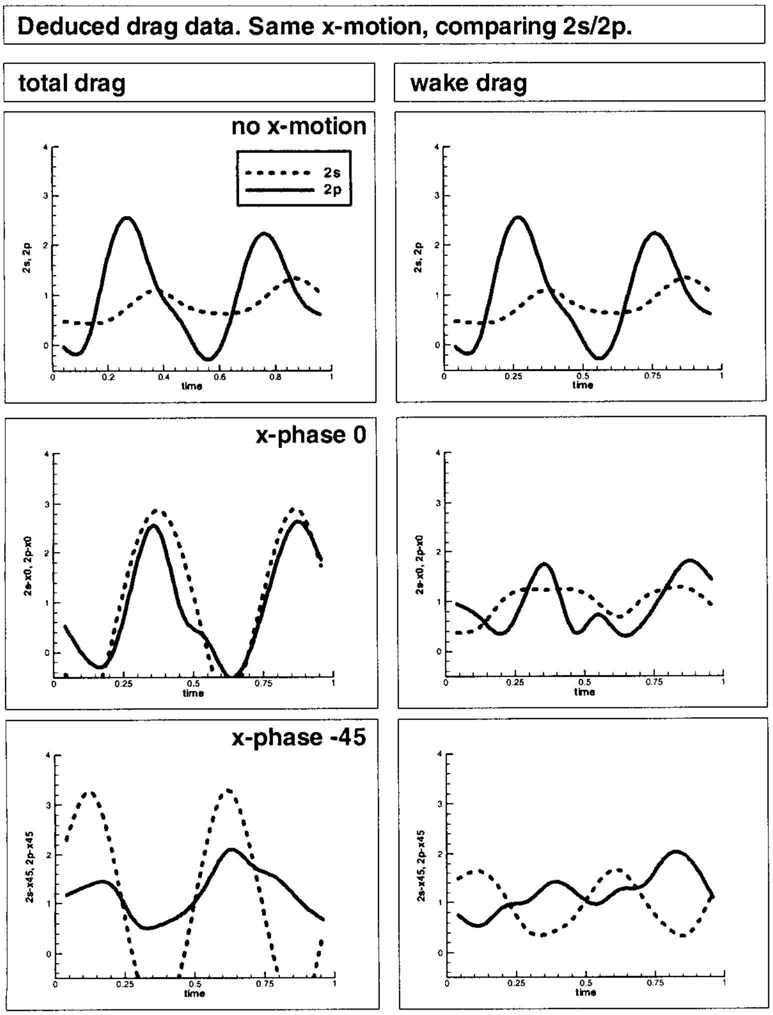

*Figure 5.2.1 - Deduced drag forces for the oscillating cylinder.*

## 5.2 Forces on the oscillating cylinder.

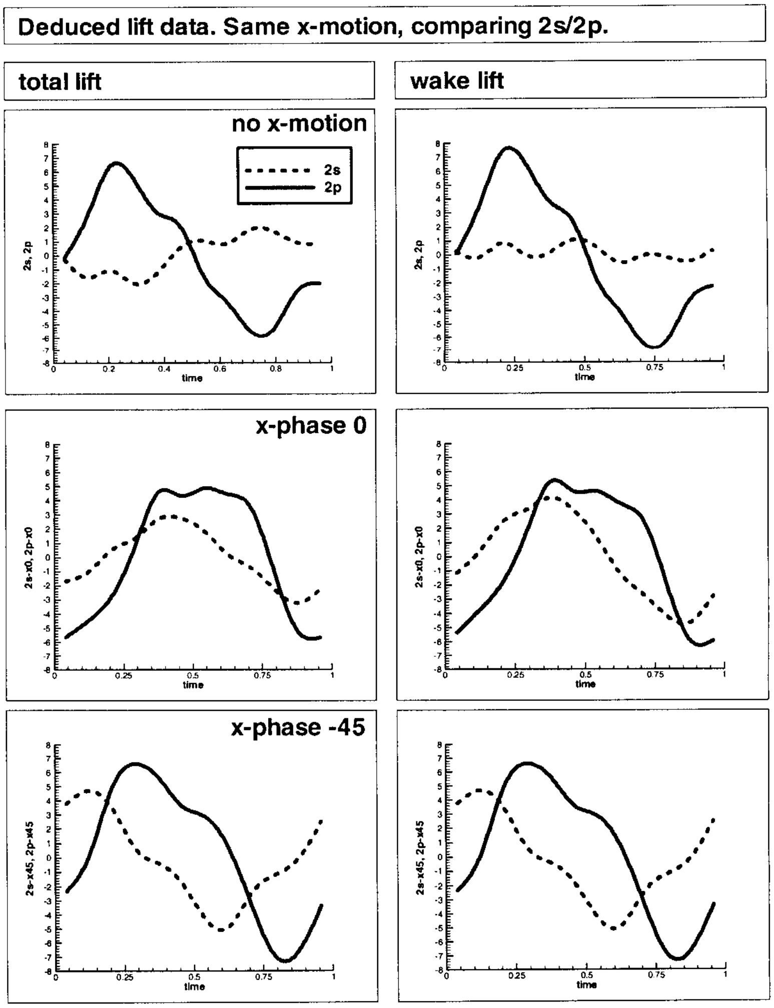

*Figure 5.2.2 - Deduced lift forces for the oscillating cylinder.*

To study the overall effect of the wake, a look at the forces on the cylinder is illuminating. Since the fluid dynamic forces represent the sum effect of all the fluid in its vicinity, it is a quick way of understanding what a given wake configuration does. Shown in figures 5.2.1-5.2.2 are the deduced forces on the cylinder, obtained by the phase averaged force deduction formula described in section 2.4. For clarity the forces with and without the inertia (i.e., added mass) force are plotted. By splitting the inertia forces from the wake forces, it offers a clearer way to see the effect of the wake dynamics by itself.

Perhaps the most glaring effect is the difference in the wake component of the lift force between the two 1-DoF cases. It is almost as if the 2S wake does nothing while the 2P wake is very active. (The very high values from the 2P case are likely due to the sectional nature of this force measurement technique. See appendix A.) It is worth noting that the expected phase relation between the total lift force and the motion is recovered. Hence it is as if in the 2S case, most of the forces are from the exertion required to move the cylinder, whereas in the 2P case the wake is positively coupling to the motion. (I.e., 2P gains power from the wake, 2S loses power to the wake.)

However, once the streamwise motions are added, there is much less difference between the different frequencies. The large amplitude difference is considerably shrunken, as is the large phase difference. The ability to control the phase of the force with the streamwise motion is also apparent. Advancing the motion causes a marked phase advancement of the forces. It is worth noting that the -45° motion does produce a lift curve more in phase with the motion than at 0° phase. Presumably nature would therefore settle upon a phase relation close to -45°.

Unfortunately, in no case does there appear to be a significant decrease in mean drag. Every case seems to show an average drag coefficient near one, with only greater or lesser fluctuations.

### 5.3 Trajectory of attached vortices in the near wake.

To better understand the behavior of the wake, a detailed study of the positions and strengths of the attached vortices in the wake of the cylinder was undertaken. Figure 5.3.1 shows the results of this study. Plotted are the spatial locations of the attached vortices, with the symbols roughly scaling with the strength of the circulation of the vortex at that time. (Circulation was computed by area integration inside manually selected contours. The ability to compute area integrals was added to the DPIV software as part of this thesis.) The numbers beside the traces indicate the time in the phase that corresponds to that point. Since the vortex is only shown when it seems to be attached to the cylin-

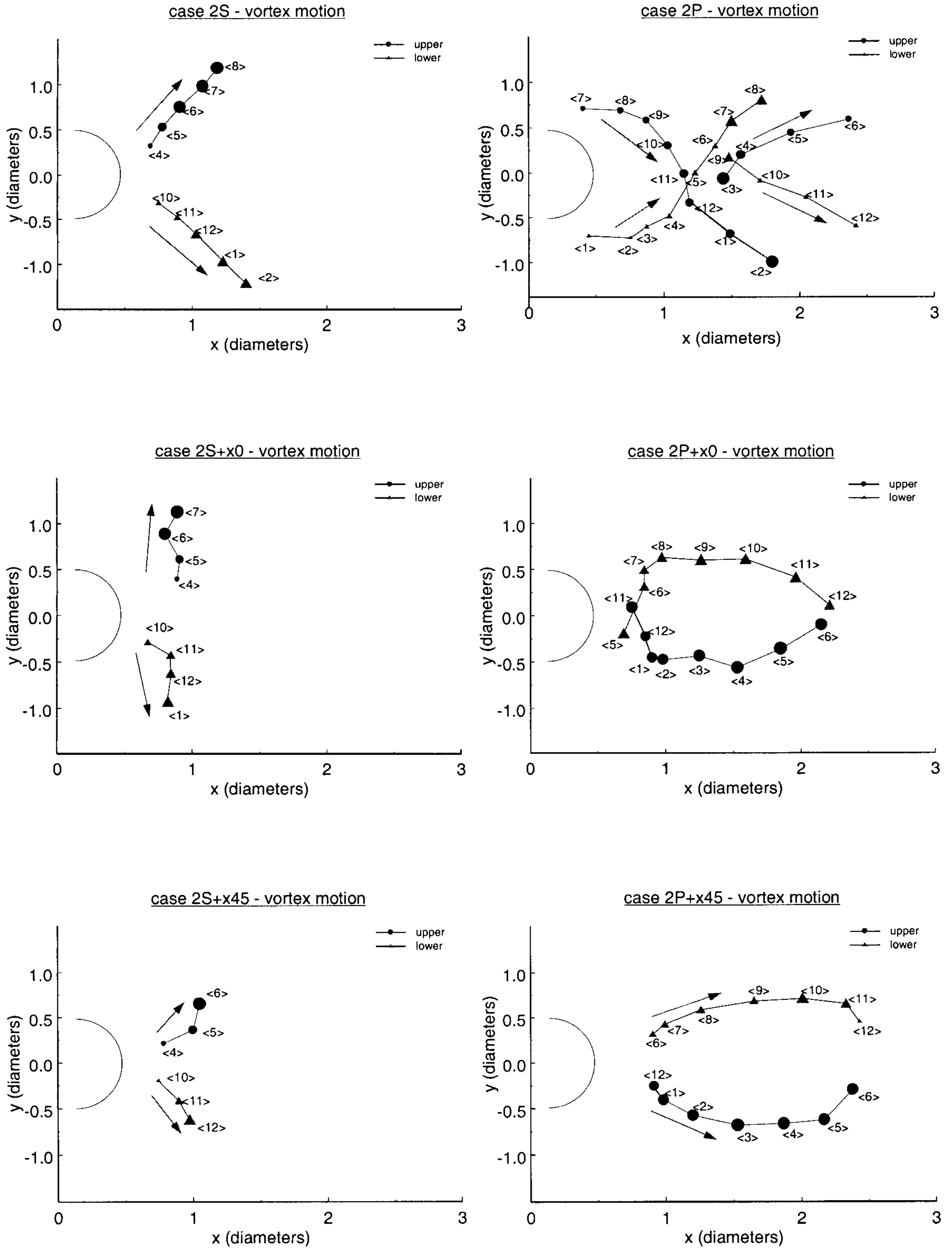

case 2S - vortex motion

case 2P - vortex motion

case 2S+x0 - vortex motion

case 2P+x0 - vortex motion

case 2S+x45 - vortex motion

case 2P+x45 - vortex motion

*Figure 5.3.1 - Vortex trajectories in the wake of an oscillating cylinder. Number indicates point in phase. Hence numbers cycle from 12 to 1 in sequence. Vortices are shown only while they are attached to the cylinder. Only the 1-DoF 2P case has two vortices per side that shed; hence, the double tracks of vortices.*

der, if only five points are shown per side, it means that the vortex was attached for only $5/12^{th}$ of the cycle. Note that the spatial coordinates are taken in cylinder fixed coordinates.

Starting with the simplest case, the 2S mode, this plot shows that the vortices form on the side they originate from (upper side vortex - negative circulation - stays on the upper side and vice versa). There is a general outward motion due to the cylinder motion. For this case, the vortex forms near one extreme of the motion and sheds near the time it reaches the opposite extreme. This is not altogether surprising behavior, as one might expect that vortices would shed near the extrema of the motion (when the lateral acceleration is strongest).

When streamwise motion is added, one is first drawn to the marked decrease in the attached time of the vortex. Looking at figures 5.1.2 and 5.1.3, it appears that the cylinder simply ejects the vortices. This is likely due to the faster formation rate from the streamwise motion. The forward acceleration occurred about the time of the shedding, which seems to short circuit formation and leads to quick ejection. Alternatively, the forward acceleration causes the cylinder to run away from the vortex, a process which hastens shedding. Other than the residence time, the formation process is essentially the same as the 1-DoF 2S case.

If one then looks at the 2-DoF cases at longer wavelength (2P + streamwise), one sees two fairly noticeable changes: increase in time and flipping of the formation side. The formation time is nearly double that of the equivalent 2S case. This is all the more interesting because in both cases, the cylinder sheds one vortex per side per cycle. And more so because the equivalent cases feature vorticies of nearly identical circulation, meaning the circulation generation rate is nearly double on the 2S side. A simple change in frequency results in a dramatic change in the time it takes for a vortex to form and shed. Equally interesting is that the vortex forms on the "wrong" side, i.e., the vortex from the upper side spends virtually all of its formation time on the lower half of the cylinder. By comparing the phase times of the vortices, one sees that at the shorter wavelengths, the upper vortex both forms and sheds on the downward stroke and vice versa for the lower vortex. In contrast at longer wavelengths, the upper vortex forms on the downward stroke, but does not shed until the upward stroke.

Saving the most complex diagram for last, one can see the pairing behavior in the 2P diagram. Note the two long S-shaped vortex paths (7..2 & 1..8). These are the tracks of the dominant vortex in the pair. Before this vortex sheds, a secondary vortex forms on the long shear layer that attaches it to the cylinder. This secondary vortex then pairs up with the opposite signed primary and is carried off downstream. Because it follows the opposite signed primary, this secondary vortex turns away from its primary and sheds in a different direction than its original course. Since the primary vortex appears to control the path of the pair, this implies that the 2P mode is really more of a 2S+s mode, where each side sheds a primary vortex and a secondary one that tags along with the opposite signed primary. This case shows the very longest of formation times, nearly three-quarters of a cycle. As with the 2-DoF cases, the primary upper vortex begins formation on the upward stroke, but does not shed until the end of the downward stroke.

### 5.4 Formation time for an oscillating cylinder.

An argument based on the path distance travelled was presented in §2.3 which suggested that at longer wavelengths the wake passes into an over-saturated state. In both the vortex ring and starting cylinder flows, it has been observed that this over-saturated state looks like a vortex with a trailing shear layer. Hence one might expect a similar behavior in the oscillating case, if in fact there is a saturation happening. This type of behavior is indeed present. Compare the shape of wake vortices in figures 5.1.2 & 5.1.5. In the 2S case (5.1.2) the vortices are round with the barest shear layer connecting them to the cylinder. In the 2P case (5.1.5) the vortices are long, with a clear head and tail morphology. To better illustrate this transition, these three flows are presented in figure 5.4.1. As noted in §5.3, the actual formation time difference between the 2S and 2P sides are fairly large.

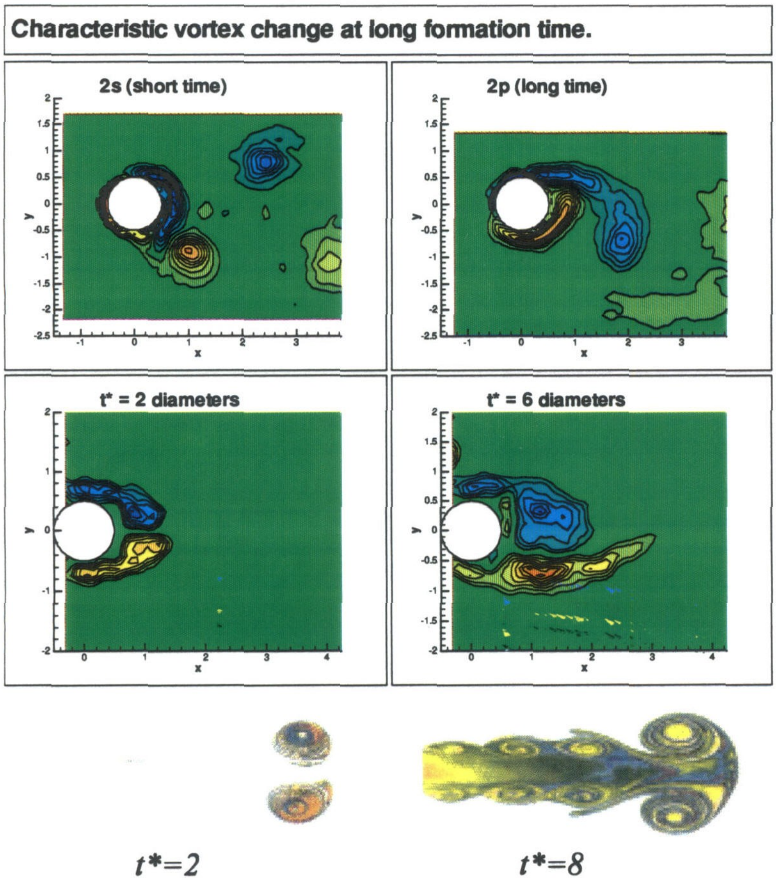

*Figure 5.4.1 - Comparison of vortices at long and short formation time. Top: oscillating cylinder. Middle: starting flow. Bottom: vortex ring (Gharib, et al., 1998).*

Note, also, the circulation values of these vortices. Recall from §5.1 the similarity in vortex strength (circulation) for any given class of motion. For example, if one looks at the peak circulation values in figures 5.1.3 & 5.1.6 – cases which differ only in frequency of motion – one finds values of 2.2 and 2.3, respectively. Although the values are nearly the same, the frequency in 5.1.6 is about 30% lower than in 5.1.3. However, like the vortex ring, the total circulation tells a different story. If one were to look at the circulation in the vortex and its trailing shear layer (the total amount produced during formation), there would be considerably more circulation in 5.1.6 than in 5.1.3. This situation is similar in the other two pairs of results.

If one compares figures 5.1.1 & 5.1.4 (transverse-only cases), one can directly see how much extra circulation is present. In the lower frequency case (2P), the extra circulation in the trailing shear layer appears to roll up and become the secondary vortex. This vortex, although weaker than the primary, still has about 85-90% of the circulation of the primaries. Hence it would appear that the vortices behind an oscillating cylinder have a critical circulation, beyond which extra circulation from the cylinder ends up in a trailing shear layer rather than the vortex. The notion of formation time seems to play an important role in determining the wake morphology of the oscillating cylinder, primarily through this critical circulation phenomena.

### 5.5 Origin of phase change of the wake.

The more fundamental question concerning the phase transition in the wake can now be addressed. It has been presumed that this change is due to a transition between two distinct wake modes, i.e., the Williamson & Roshko (1988) 2S & 2P modes. Williamson & Roshko suggest that this transition happens because of the timing of vortex formation. They suggest that during the acceleration phase of the motion, the wake always generates two vortices per side, and the wavelength selects whether one or two of these vortices will be shed per side. Blackburn & Henderson (1999) suggest that this phase change comes from competition between vorticity generation by the body motion and the pressure gradient on the body. They suggest that at different frequencies the shear layer on one side of the body is preferential fed. Bishop & Hassan (1964) seem to only report that the phase change exists and do not speculate on its origin. Ongoren & Rockwell (1988) comment on the morphology of the wake near the phase shifting point, but not on the origins of this behavior.

The astute reader would have deduced from the previous sections that this transition seems to arise from formation time effects. The important change in the wake is that it is exceeding the critical time (i.e., the distance travelled by the stationary cylinder per cycle) causing the vortex morphology to change from vortex to vortex-and-tail. By allowing the vortices to remain attached beyond the critical time, the wake transitions from forming and shedding on the same direction of motion to

| | Rising | | | Falling | | | | | | Rising | | | | | | Falling | | | | | | Rising | | |
|---|---|---|---|---|---|---|---|---|---|---|---|---|---|---|---|---|---|---|---|---|---|---|---|---|
| Phase | 1 | 2 | 3 | 4 | 5 | 6 | 7 | 8 | 9 | 10 | 11 | 12 | 1 | 2 | 3 | 4 | 5 | 6 | 7 | 8 | 9 | 10 | 11 | 12 |
| 2S | ▨ | ▨ | ▨ | upper | | | | | ▨ | ▨ | ▨ | ▨ | ▨ | ▨ | ▨ | upper | | | | | ▨ | ▨ | ▨ | ▨ |
| | | | ▨ | ▨ | ▨ | ▨ | ▨ | ▨ | ▨ | lower | | | | | ▨ | ▨ | ▨ | ▨ | ▨ | ▨ | ▨ | lower | | |
| 2S + x0 | ▨ | ▨ | ▨ | upper | | | | ▨ | ▨ | ▨ | ▨ | ▨ | ▨ | ▨ | ▨ | upper | | | | ▨ | ▨ | ▨ | ▨ | ▨ |
| | | ▨ | ▨ | ▨ | ▨ | ▨ | ▨ | ▨ | ▨ | lower | | | | ▨ | ▨ | ▨ | ▨ | ▨ | ▨ | ▨ | ▨ | lower | | |
| 2S + x45 | ▨ | ▨ | ▨ | upper | | | ▨ | ▨ | ▨ | ▨ | ▨ | ▨ | ▨ | ▨ | ▨ | upper | | | ▨ | ▨ | ▨ | ▨ | ▨ | ▨ |
| | | ▨ | ▨ | ▨ | ▨ | ▨ | ▨ | ▨ | ▨ | lower | | | ▨ | ▨ | ▨ | ▨ | ▨ | ▨ | ▨ | ▨ | ▨ | lower | | |
| 2P primary | | | ▨ | ▨ | ▨ | ▨ | upper | | | | | | | | ▨ | ▨ | ▨ | ▨ | upper | | | | | |
| | lower | | | | | | | | ▨ | ▨ | ▨ | ▨ | lower | | | | | | | | ▨ | ▨ | ▨ | ▨ |
| 2P secondary | ▨ | upper | | | | | ▨ | ▨ | ▨ | ▨ | ▨ | ▨ | ▨ | upper | | | | | ▨ | ▨ | ▨ | ▨ | ▨ | ▨ |
| | ▨ | ▨ | ▨ | ▨ | ▨ | ▨ | ▨ | lower | | | | | ▨ | ▨ | ▨ | ▨ | ▨ | ▨ | ▨ | lower | | | | |
| 2P + x0 | ▨ | ▨ | ▨ | ▨ | upper | | | | | | | | ▨ | ▨ | ▨ | ▨ | upper | | | | | | | |
| | | | | | | | ▨ | ▨ | ▨ | ▨ | lower | | | | | | | | ▨ | ▨ | ▨ | ▨ | lower | |
| 2P + x45 | ▨ | ▨ | ▨ | ▨ | ▨ | upper | | | | | | | ▨ | ▨ | ▨ | ▨ | ▨ | upper | | | | | | |
| | | | | | | | ▨ | ▨ | ▨ | ▨ | ▨ | lower | | | | | | | ▨ | ▨ | ▨ | ▨ | ▨ | |

*Figure 5.5.1 - Phases of motion during which a vortex is attached to the cylinder. The phases are further deliniated according to whether the cylinder is rising or falling. By looking at the times the vortices are formed and shed, one can see how increased formation time can lead directly to an apparent phase change.*

forming and shedding on opposite strokes. When the vortex that forms on the upper side on the downward stroke sheds on the upward stroke, the wake has, in effect, flipped over. Now it appears that the "outside" vortex is shedding rather than the "inside." Therefore, prolonging the formation process seems to be enough to flip the phase of the wake. Figure 5.5.1 illustrates this concept graphically. For example, examine the middle section, during which the cylinder is rising. In every case, the cylinder begins the formation of a vortex on the lower side (positive circulation). However, the three shorter formation time cases also shed this vortex within the rising stroke, whereas the longer formation time cases shed them on the following falling stroke. Without the change in morphology, the wake would likely eject the vortex at the formation time, in which case the vortex would also shed on the stroke it formed on. After all, at the end of a stroke, there is a strong acceleration event which would cut off the vortex. The vortex-and-tail morphology seems to be necessary for the vortex to stay attached beyond the extrema of the motion, without which the phase transition would likely disappear.

Furthermore, without quantitative data, the importance of formation time would be difficult to ascertain. As an example, if one used dye visualization to obtain figure 5.4.1, one would likely see the vortices, but would be unable to tell if a shear layer or a trail of dye connected them back to the cylinder. Without that datum, one would be left to work out the phase transition from just the timing of the vortices. And, of course, one has to think of wake dynamics in terms of critical formation times.

That the flipping of the wake is enough to cause the phase transition is illustrated below. Again start with the impulse formulation,

$$\mathbf{F} = \frac{d}{dt}(\rho \int \mathbf{x} \times \omega \, dV) \qquad \text{(eq. 5.5.1)}$$

Taking the component in the lift direction, and reducing the wake to the single most dominant vortex, this becomes

$$lift \approx -\frac{d}{dt}(\rho x \Gamma) = -\rho(\Gamma \dot{x} + x \dot{\Gamma}) \qquad \text{(eq. 5.5.2)}$$

where Γ refers to the circulation of that vortex and x its position downstream from the cylinder. Since both x and the circulation are constantly rising during the formation process, the sign of the lift force is determined by the sign of Γ relative to the motion of the cylinder. (See direction of vortex trajectories in fig. 5.3.1.) To get positive coupling, the dominant vortex in the wake must be negative on the rising stroke, since a positive x crossed with a negative Γ points in the positive y direction. Therefore, exceeding the critical formation time causes the wake to move into the opposite shedding state which results in a positive coupling between the wake forces and the cylinder motion.

Furthermore, because a passive structure can only draw energy from the wake, a cylinder in lock-in must necessarily lock at a frequency less than or equal to the Strouhal frequency. (See Blackburn & Henderson, 1999, about energy transfer to and from the wake based on direction the cylinder travels in phase space.) For comparison, the average power required to move the cylinder traversely was computed. For 1-DoF motions, the higher frequency case (2S) feeds 1.2 units of power into the wake while the lower frequency case (2P) receives 1.6 units. When the streamwise motion is added, the situation becomes more interesting. At 0° phase, the power is reversed, with the lower frequency case losing 0.45 units while the higher frequency case gains 1.0 units. And at -45°

phase, both cases gain power, but the higher frequency case gains much less (0.31 units vs. 2.8 units). The effects of streamwise motion are again evident. Changing the phase of the streamwise motion radically alters the energy flow, even to the point of reversing the sign. And the very large transfer from the wake for the -45° case implies that this motion is more favored than the 1-DoF motion.

In a sense, it is a string of coincidences that leads to the strong coupling of the structure to its wake. Energy arguments select lower frequencies, which are necessarily at longer formation time. This leads to a change in the morphology of the wake which allows the vortices to remain attached long enough to switch the phase of shedding and hence the force. If it were not for the changing morphology as the critical formation time is exceeded, the strong fluid-structure coupling might not materialize since the fluid forcing and the structure motion would have the wrong phase relationship.

### 5.6 2P, the Red Herring? *

The last issue then is to address the nature of the pairing mode. It seems almost arbitrary that the wake would suddenly choose to produce two vortices per side in a cycle rather than the customary one vortex. The hypothesis presented here is that the second vortex in the pair is produced by a different mechanism than the first. The first vortex is produced in the manner of Kármán vortex shedding, and the second is formed when the shear layer attaching it to the cylinder has a secondary roll-up. This process is only available at low acceleration/low circulation production rates; at high acceleration, the vortex forms and sheds too quickly for the secondary roll-up. As shown in §4.3, if one accelerates a

---

* Red Herring - something that distracts attention from the real issue (from the practice of drawing a red herring across a trail to confuse hunting dogs). Merriam-Webster Dictionary.

cylinder from rest sufficiently slowly, the wake develops in a very symmetrical fashion. For the oscillating cylinder, it seems that if the acceleration is low, the forming vortex is allowed to remain attached to the cylinder too long, which leads to an unusually long trailing shear layer. This shear layer then rolls up into a second vortex before the first one actually sheds. As with the starting case, this also leads to what looks like a very long wake as the wake is too stable to quickly eject the forming vortex. This process is also analogous to the vortices forming on the trailing jet behind a long formation time vortex ring (see figure 5.4.1).

In addition, one can look at the effect of altering the acceleration on the wake pattern. This is easily achieved with this experimental equipment since there is an extra degree of freedom with which to increase or decrease the formation time. For example, if streamwise motion at 0° phase is added to the transverse motion, a little extra acceleration is injected in the middle of the formation process. The result is a shift back to a single vortex mode (see figure 5.1.5). This acceleration speeds up the formation process and the long shear layer does not have the time to roll up. On the other hand, if streamwise motion at 180° phase is added, a little deceleration is injected in the middle of the formation process. This should, therefore, result in more time to roll up. As shown in figure 5.6.1, this results in what one might call a 2T (two triple) mode as the wake now has the time to form even a third vortex on that shear layer before shedding. It would seem that the pairing mode is indicative of being in a low acceleration regime, rather than causing a change by itself. In a sense, the more correct long wavelength behavior is the vortex-and-tail mode (which is half of the 2P mode). However, using non-quantitative flow visualization, one could not tell that both vortices of the

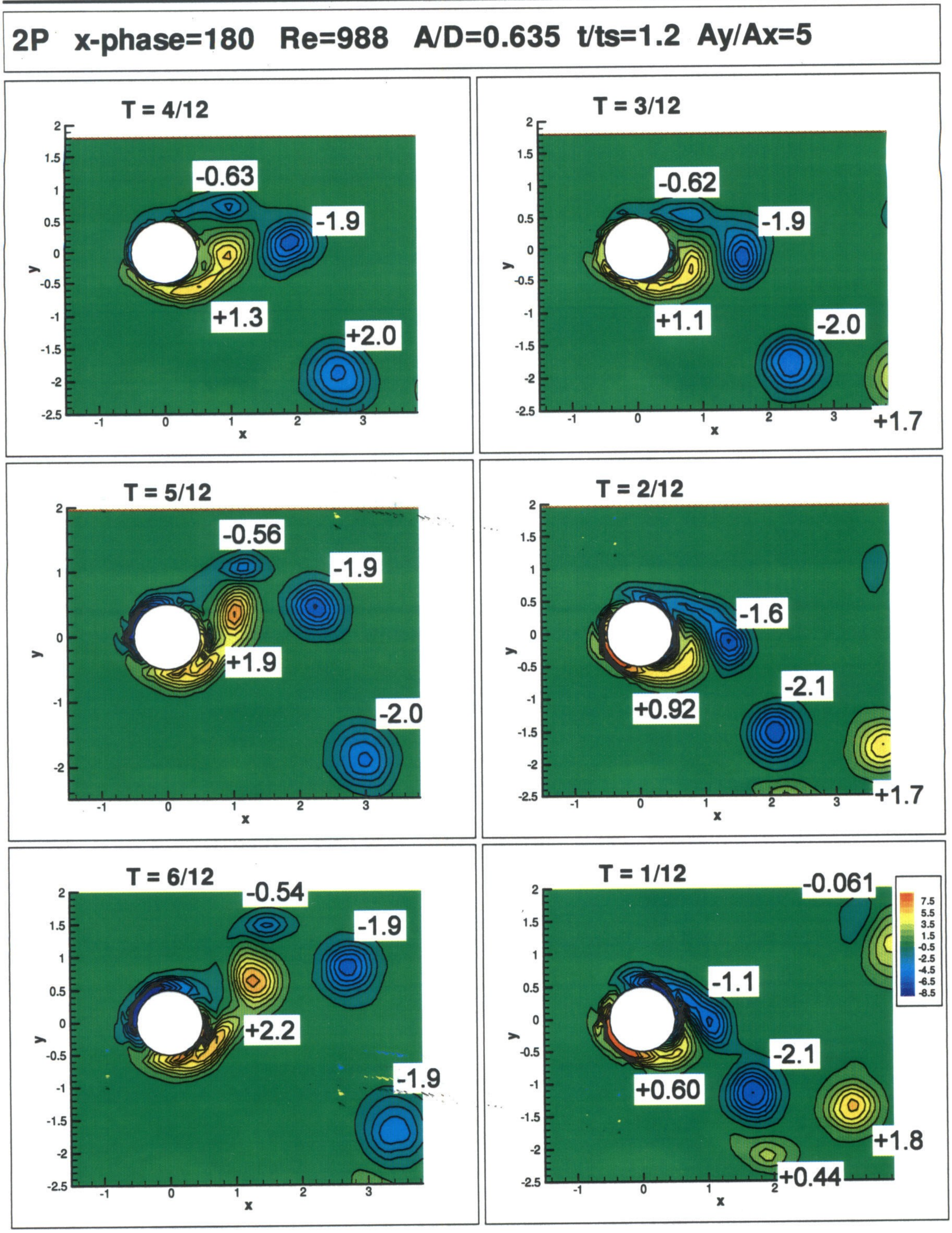

*Figure 5.6.1 - Phase averaged vorticity for transverse motion in the 2P region with streamwise motion at 180 degrees phase. Upper half cycle of motion. Note the trio of vortices shed from each side per cycle. The shear layer has time to form two vortices before shedding. Numbers indicate circulation of vortex.*

**Changes in vortex formation with varying formation via acceleration.**

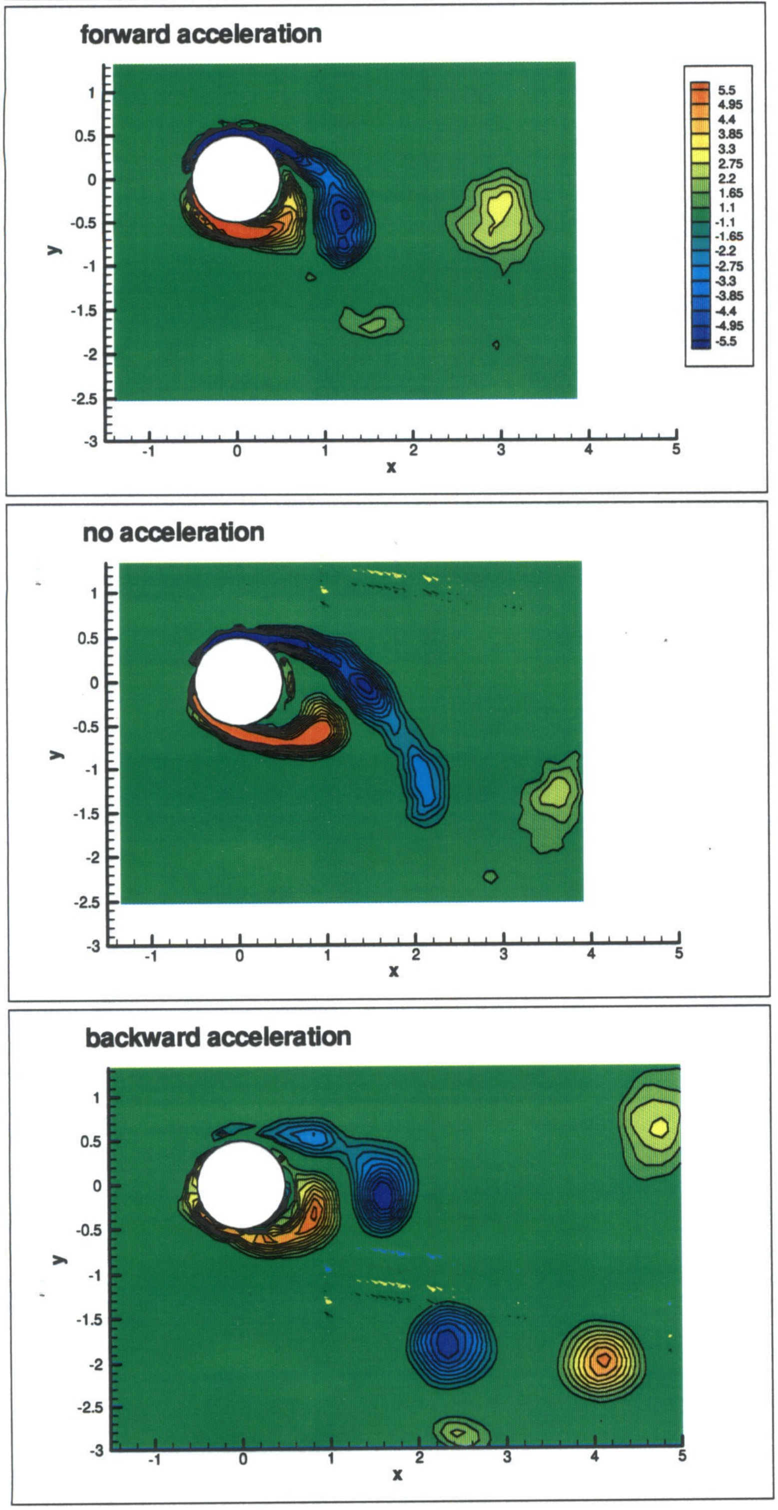

*Figure 5.6.2 - Family of wake modes generated by altering formation time via streamwise motion.*

2P are attached to the cylinder at the same time on the same shear layer. Not knowing that, it would seem, perhaps, that one might easily conclude that the first half of the pair had shed long before the second, and that the two vortices had formed independently.

Furthermore, this might also go part way toward explaining why not all researchers find the pairing mode. After all, if the transition from single to paired vortices is sensitive to the formation rate and time of the vortex, then amplitude and wavelength would not uniquely determine the shedding mode. The usual amplitude and wavelength parameters would directly affect the primary vortex, but the formation of the secondary vortex would depend on the shear layer trailing from the primary. Hence amplitude & wavelength would not uniquely determine if secondary vortices should form and shed. If the Reynolds number is too low, the trailing shear layer might be too stable to roll up in time to form the second vortex. Likewise, if the noise in the system is too low, the shear layer might not have enough perturbation to begin the second roll up. On the other hand, parasitic vibrations might switch one from what would have been a pairing mode into a single. A quiet facility like the towing tank, coupled with free surface visualization (the free surface tends to stabilize vortex formations), could allow the shear layer enough time to form the second vortex. And a low Reynolds number computation might never see it because the shear layers would be too stable. In practice, it seems unlikely that the pairing mode would be common in the actual application; there would be too much vibration, noise, and streamwise acceleration to expect something so fragile to be found in practice. Rather the interesting physics seems to be related to the formation time and accompanying morphology change.

# 6

# Conclusions

The role of formation time in vortex formation is illustrated for two types of bluff body flows. First demonstrated for vortex ring formation, the idea has been extended to the formation of vortices in the wake of a cylinder. When a cylinder is started from rest, the critical time is around four diameters, at which time the wake becomes strongly asymmetrical and starts the shedding process. For a cylinder in oscillatory motion, the critical time is around five diameters, the time when the stationary cylinder sheds (as per the Strouhal period). Crossing the critical time leads to a change in wake morphology, which in turn allows a phase reversal in the wake.

The starting flow is characterized by a pair of symmetrical vortices in the near wake. The breakdown of this symmetry is the key event in the transition between the starting flow and the steady-state vortex shedding. This symmetry breaking was demonstrated to occur around a time of four diameters – the same time when the wake vortices reach the level of circulation present in the first shed vortex. This process seems to be initiated by vorticity annihilation in the wake, evidence of which is visible in the early time force data. A more direct method for measuring the asymmetry in the wake was also presented. From the exponential growth of asymmetry, it is presumed that a linear instability in the wake leads to the symmetry breaking.

The oscillating flow is characterized by vortex shedding locked to the motion of the cylinder. However, when the motion exceeds the critical formation time, the wake switches morphology (from vortex to vortex-and-tail). This change allows the formation process to be extended long enough for the wake to switch phase. A direct connection was shown between the formation time and the phase of shedding. The wake appears to change phase when the formation process extends past the extrema of motion, such a vortex forming on the falling stroke shedding on the rising stroke, instead of forming and shedding on the same stroke. In turn this switch in phase allows the wake to positively couple with the cylinder motion at low motion frequencies. Lastly it was shown how the vortex-and-tail morphology behaves like a vortex and attached shear layer. This shear layer can then roll-up to form extra vortices, leading to the appearance of extra vortices shed per cycle.

This formation process can be altered by the addition of streamwise motion. For example, when the streamwise motion is such that the cylinder is moving forward at the extrema of motion, the formation process is hastened. This hastening appears to keep the wake from going into the 2P wake mode described by Williamson & Roshko (1988). Likewise streamwise motion in the opposite direction has been shown to increase the formation process, leading to the formation of extra vortices per cycle due to a secondary roll-up of the trailing shear layer. In addition, it was shown that the streamwise motion seemed to increase phase coherency of the wake, presumably by further coordinating the phase of vortex formation. This coordination is strong enough to significantly alter the phase of the wake, such that a 45° degree phase shift in the streamwise motion results in nearly a one diameter shift in the positions of the vortices in the wake.

The work of Noca, et al. (1997) on force deduction from velocity field data was extended for strongly phase coherent flows. Since forced oscillating cylinder flows are strongly phase coherent, this technique proved useful for force measurement. In essence, a phase-time averaged version was developed that trades time resolution for accuracy, without losing all of the dynamics. Hence reasonable force measurements were taken using the measured velocity fields, even though the data would be considered too coarse (both spatially and temporally) for the time-resolved technique.

In the future the underlying physics behind the vortex to vortex-to-tail transition should be explored further. Understanding this process would likely explain why the Strouhal number is so close to 0.2 across many orders of magnitude of Reynolds number. And once the technology becomes available, this work should be revisited at a higher temporal and spatial resolution. Then the fully time-resolved force deduction technique could be employed. However, this would require at least ten times the temporal and spatial resolution, in addition to measuring the full three-component velocity field.

# References

Barkley, D. & R. D. Henderson. *Three-dimensional Floquet stability analysis of the wake of a circular cylinder.* Journal of Fluid Dynamics. vol. **322** (1996) : pp. 215-241.

Bearman, P. W. *Vortex Shedding from Oscillating Bluff Bodies.* Annual Review of Fluid Mechanics. vol. **16** (1984) : pp. 195-222.

Bernard, H. *Formation de Centres de Giration a l'Arriere d'un Obstacle en Mouvement.* Comp. Rend. Acad. Sci. Paris. vol. **146**. (1908).

Bishop, R. E. D. & A. Y. Hassan. *The Lift and Drag Forces on a Circular Cylinder Oscillating in a Flowing Fluid.* Proceedings of the Royal Society (London). Series **A 277**. (1964) : pp. 51-75.

Blackburn, H. M. *Sectional lift forces for an oscillating circular cylinder in smooth and turbulent flows.* Journal of Fluids & Structures. vol. **11** (1997) : pp. 413-431.

Blackburn, H. M. & R. D. Henderson. *A study of two-dimensional flow past an oscillating cylinder.* Journal of Fluid Dynamics. vol. **385** (1999) : pp. 255-286.

Blevins, Robert. Flow-Induced Vibration. San Francisco: van Nostrand Reinhold Company, 1977.

Bouard, R. & M. Coutanceau. *The early stage of development of the wake behind an impulsively started cylinder...* Journal of Fluid Dynamics. vol. **101** (1980) : pp. 583-607.

Den Hartog, J. P. *The Vibration Problems in Engineering.* Proceedings of the 4th International Congress on Applied Mechanics. Cambridge, U.K. : pp. 36-53. (As referenced in Zdravkovich, 1982.)

Feng, C. C. *The measurement of vortex-induced effects in flow past a stationary and oscillating circular and D-section cylinders.* M.A.Sc. thesis, University of British Columbia (1968). (As published in Parkinson, 1989.)

Gharib, M., E. Rambod, & K. Shariff. *A Universal Time Scale for Vortex Ring Formation.* Journal of Fluid Mechanics. vol. **360** (1988) : pp. 121-140.

Honji, H. & S. Taneda. *Unsteady flow past a circular cylinder.* Journal of the Physical Society of Japan. vol. **27**, no. 6 (1969) : pp.1668-1677.

Karman, T. *Über den Mechanismus des Widerstandes den ein bewegter Körper in einen Flüssigkeit Erfahrt.* Göttingen Nachr. Königl. Gesselschaft. (1912). 547.

Koumoutsakos, P. & A. Leonard. *High-resolution simulations of the flow around an impulsively started cylinder using vortex methods.* Journal of Fluid Mechanics. vol. **296** (1995) : pp. 1-38.

Merriam-Webster. WWWebster Dictionary. Merriam-Webster Online, Inc. (2000). http://www.m-w.com.

Morton, B. R. *The Generation and Decay of Voriticty.* Geophysical & Astrophysical Fluid Dynamics. vol. **28** no 3-4 (1984) : pp. 277-308.

Noca, F., D. Shiels, & D. Jeon. *Measuring Instananeous Fluid Dynamic Forces on Bodies Using Only Velocity Fields and Their Derivatives.* Journal of Fluids & Structures. vol. **11** (1997) : pp. 345-350.

Noca, F., D. Shiels, & D. Jeon. *A Comparison of Methods for Evaluating Time-Dependent Fluid Dynamic Forces on Bodies, Using Only Velocity Fields and Their Derivatives.* Journal of Fluids & Structures. vol **13.** (1999) : pp. 551-578.

Norberg, C. *An experimental investigation of the flow around a circular cylinder: influence of aspect ratio.* Journal of Fluid Mechanics. vol. **258** (1994) : pp. 287-316.

Parkinson, G. *Phenomena and Modelling of Flow-Induced Vibrations of Bluff Bodies.* Progress in Aerospace Science. vol. **26** (1989) : pp. 169-224.

Saffman, P. G. Vortex Dynamics. Cambridge, U.K. : Cambridge University Press, 1992. pp. 46-53.

Sarpkaya, T. *Vortex-Induced Oscillations: A Selective Review.* Journal of Applied Mechanics. vol. **46** (1979) : pp. 241-258.

Strouhal, V. *Uber eine besondere Art der Tonerregung.* Ann. Physik (Leipzig), 1878.

Szepessy, S. & P. W. Bearman. *Aspect ratio and end plate effects on vortex shedding from a circular cylinder.* Journal of Fluid Mechanics. vol. **234** (1992) : pp. 191-217.

Taneda, S. *Experimental Investigation of the Wakes Behind Cylinders and Plates at Low Reynolds Numbers.* Journal of the Physical Society of Japan. vol. **11**, no. 3 (1956) : pp. 302-307.

Westerweel, J., D. Dabiri, & M. Gharib. *The effect of a discrete window offset on the accuracy of cross correlation analysis of digital PIV recordings.* Experiments in Fluids. vol. **23** (1997) : pp. 20-28.

Willert, C.E. & M. Gharib. *Digital Particle Image Velocimetry.* Experiments in Fluids. vol. **10** (1991) : pp. 181-193.

Williamson, C.H.K. & A. Roshko. *Vortex Formation in the Wake of an Oscillating Cylinder.* Journal of Fluids and Structures. vol. **2** (1988) : pp. 355-381.

Zdravkovich, M. M. *Modification of Vortex Shedding in the Synchronization Range.* Journal of Fluids Engineering. vol. **104** (1982) : pp. 513-517.

# Appendix A

# Experimental Validation of Force Deduction

Plotted below in figure A1.1 is a comparison between the deduced force and the measured force using the force balance. The deduced force data only covers one cycle; they are duplicated for comparison purposes. There are several reasons for the discrepancy between the force amplitudes. Some are errors associated with deficiencies in the experimental setup, while others come from real differences in measurement.

The most obvious source of error is insufficient resolution in the DPIV system. For example, the video system is limited to 30 Hz, which translates into only 15 data sets per second or approximately 33 sets per cycle. The interrogation window, while more than sufficiently small to capture wake vortices, is too large to measure the details of the cylinder boundary layers. However, the use of the phase averaged technique is designed to minimize the effects of low resolution so these errors are not likely to be large. An

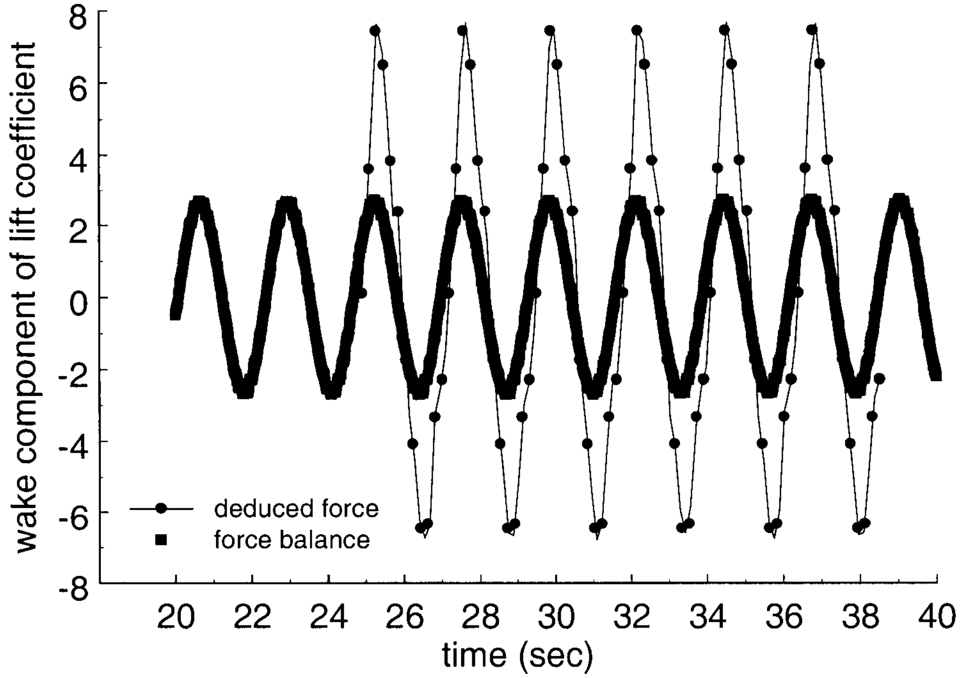

*Figure A1.1 - Comparison between phase-averaged deduced force and experimentally measured forces from the force balance. Deduced force data are only one cycle long and are duplicated for comparison.*

unknowable source of error is that the current DPIV system can only measure velocities in a single plane. Ideally one needs full three component data and gradients. The current implementation of the force deduction simply ignores the unmeasurable quantities. For this case, the flow is strongly two-dimensional (see Blackburn, 1997). As a result this, too, is unlikely to contribute a large amount of error.

There are also errors associated with calibration of the force balance. Although the balance was carefully calibrated statically, it is difficult to get an accurate calibration for the moving balance. This is due to the difficulty in applying a known force to a moving balance. Again, this difference should be small since the natural frequency of the balance is significantly higher than the motion frequencies and the system is well damped.

The remaining source of discrepancy is the difference between measuring sectional and spanwise-averaged forces. As detailed in Noca, et al. (1997), this difference can be quite large. Figure A1.2 is a comparison between the measured and deduced forces for a fixed cylinder, taken from Noca, et al. (1997). Here the full time-resolved formulation is used. This amplitude discrepancy is also present here. This figure illustrates one of the mechanisms by which the sectional force is in fact not the same force as the spanwise-averaged one. Note the way in which the phase of the deduced force varies against the spanwise-averaged force. Around time five the two forces are nearly 90° out of phase, while at time 20 they are nearly in phase with one another. When these gentle phase variations are averaged over the span of the cylinder, the average value of the force magnitude drops. To complicate matters, the degree to which the average value is attenuated is a function of the experimental setup. Factors like the aspect ratio of the cylinder (length / diameter) [see Norberg, 1994], end conditions, and cylinder motion all affect the three-dimensionality of the wake. Nevertheless, this illustrates that sectional and spanwise-averaged forces are not necessarily measuring the same quantity. From the above spanwise variations, one would expect the deduced forces to be higher; consequently, the apparent discrepancy is likely due to real fluid dynamic effects.

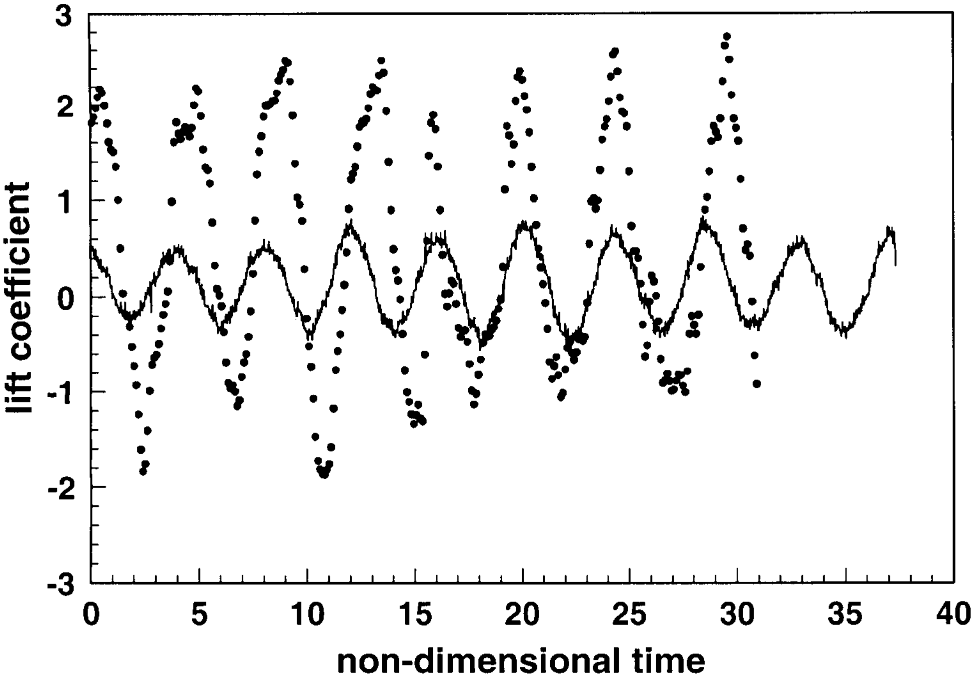

*Figure A1.2 - Comparison between time-resolved deduced force and experimentally measured force from a force balance. Note the manner in which the deduced force slides in and out of phase with the force balance signal.*

# Appendix B

# Computer Programming Projects

Several programs were either modified or created in the course of this work. They are listed below, along with a description of their use and purpose.

### * Pre-processing software *

**getpair2**

Used to download images taken on the Sony LVR using the Coreco frame grabbing board. This version was especially modified to give control over the brightness and contrast of the frame grabber's A/D convertor. This maximizes the image quality for a given run.

**tasty**

Haar wavelet based image adjustment. Tasty is used to sharpen or smooth an image, as well as equalize its brightness. Taking advantage of the compact support of wavelets, one can limit the smallest scale of mean brightness variation. The function is similar to “minmax,” which performs histogram style equalization. However, tasty is order N in pixels, making it several times faster (seconds vs minutes).

**bad_pixels**

Blank out the known bad pixels for given cameras to avoid spurious particles appearing in the image. Sets the offending pixel values to zero to avoid correlating them with real particles.

### * Processing software *

**dpiv**

Main DPIV processing software. Ported it from UNIX to Windows NT. Modified the program to accept floating point images, which some pre-processing software produced.

**smeg**

Window shifting and spatial windowing version of DPIV. Used after DPIV has already been run. Window shifting has been shown to greatly reduce the noise in the DPIV computations, largely because the number of matching particles in the two interrogation windows is increased. (See Westerweel, et al., 1997.) Smeg also performs spatial windowing (a la Hanning windows or Poisson windows) which provide both anti-aliasing and an increase in spatial resolution.

## * Post-processing software *

### nocylinder

Sets the value(s) within a specified circle to a specified value. Used to set spurious vector/scalar quantities inside the cylinder to the appropriate value. In this thesis, used to set the values inside the cylinder to that of the equivalent slug of fluid moving at the speed of the cylinder. That way the force deduction computation would not need to explicitly know the location of the cylinder.

### uncylinder

Similar to nocylinder, except backwards. Sets values for quantities outside a specified circle.

### lagrange

Shifts and rescales vector field to put it in cylinder fixed coordinates.

### rescale

Rescales data and axes and translates the field. Used center coordinate system on the cylinder and to non-dimensionalize all of the data.

## * Analysis software *

### psycho

Time statistics program. Computes averages and fluctuating quantities and various correlations. Operates on scalars, vectors, vectors with scalars, and scalars with scalars. Psycho operates on sequences of files, but can safely skip missing files – a useful feature for phase averaging.

### strouhal

Time variations at a point. Nominally designed to output the data at a given point with time, so that quantities like the Strouhal frequency can be computed. However, to test convergence, the program also outputs a running tally of the average and fluctuating components as well.

**split_field**

Splits the given vector field into the mirror symmetric and everything else fields.

**norm**

Computes the one, two, and infinity norms on a given region of a vector field. These norms are, respectively, the mean of the magnitudes, the root mean square of the magnitudes, and the largest magnitude.

**flforce**

Compute the instanteous forces on a body using the force deduction technique described in Noca, et al. (1997, 1999). Simulanteously computes the forces using several different versions of the formulation. Can also switch from forward to central differencing in time.

**flforce_ra**

Reynolds averaged version of flforce.

**pdf**

Computes a simple histogram type probability density function at a given point in the flow over time.

**smudge**

Spatial averaging. Useful for measuring the freestream speed or for reducing the spatial resolution for Large Eddy Simulation type studies where the analysis needs to performed at various scales.

**vortage**

Computes vorticity using analytical derivatives of natural splines. Considered to be a good way to compute derivatives of high order without suffering from excessive noise. Although it is more sensitive to noise than the regular vorticity computation program, it has significantly better spatial resolution.

**derivaton**

Uses the analytical derivatives of natural splines to compute other derivative quanities like strain and divergence.

**massage**

Adjust data to accommodate known problems.

*** Utility software ***

**bintoascm**

Converts a DPIV binary file into a text matrix. Some field plotting programs insist on data in matrix format rather than a list of coordinates.

**bintotec**

Converts a DPIV binary file into a TecPlot friendly text file.

*** Superscope specific software ***

**ss2text**

Converts SuperScope binary files into PC text files.

**text2ss**

Converts PC text files into SuperScope compatible binary files.

**ss_rtrend**

Removes a linear trend from SuperScope data files.

**ss2haar**

Performs a high and/or low pass Haar wavelet based filter operation on SuperScope data.

*** Stereographic PIV software ***

**triangulate**

Computes the three-component vector field given the two stereo vector field and geometry information. Compensates for both non-square grids and gridpoint-to-gridpoint variation in viewing angles.

**conerod**

Computes the mean parallax error in the in-plane field. Assumes parallax error is an elliptical cone, growing linearly from an origin. Fits a straight line to u(x) and v(y) independently since the parallax error rate is typically *different in* the two principle directions.

**unparallax**

Takes the conerod information and removes the parallax error from the three-component data.

### * Graphical software *

**vector**

Plots DPIV vector data to screen. Uses standard Win32 dialog boxes to both open and print these files. Capable of loading several files at once so that one can cycle through a sequence. Capable of displaying the data at one user-selected point in the flow. Capable of drawing 1-D slices through the vector field at a specific cut. Capable of computing various integrals on user defined contours. Capable of drawing a reference vector and reference circle (blank inside or out).

**contour**

Similar to vector, except for scalar data. Makes contour plots. For black-and-white printers, contour is able to switch its color map to solid line/dashed-line.

**dpivmenu**

DPIV processing parameters in an interactive menu. Able to read in a pair of images and perform *in situ* DPIV to test image quality and processing parameters. Reports not only the computed displacements but shows the correlation function so that the quality of the correlation can be directly evaluated. Capable of displaying the resultant vectors on the screen, superimposed on the image. Capable of displaying the location/size of the interrogation window selected for comparing the size of the window to the features or objects in the flow. Also useful as a learning tool for understanding the DPIV process.

# Appendix C
# Motion Control Source Code

```
; Motion control program for Aerotech controller software.
; Written by David Jeon via a C language program for automation.
; Designed to take maximum advantage of the Aerotech software
;   for smoothest motion.
; figure eight motion
;   amplitude (x) 1  (y) 5
;   x phase difference 0.785398
;   period 0.75 sec
;   number of steps 20
;   number of loops 20

program en ab
enable x y
DS 2,PA,0.01,4
; enable velocity profiling, preventing traverse from
; stopping at every control point
velocity on
; enable trajectory smoothing
rounding on
; sinusoidal acceleration profile between points
trajectory sine
; take 0.18 secs to change velocity
ramp 18
; take 0.09 secs to smooth trajectories around control points
rounding 9
; run motion 60 times
loop 60
linear x0.9877 y1.5451 f841.3132
linear x0.8910 y2.9389 f748.2864
linear x0.4540 y4.0451 f638.0175
linear x-0.1564 y4.7553 f504.1827
linear x-0.7071 y5.0000 f326.0747
linear x-0.9877 y4.7553 f200.7981
linear x-0.8910 y4.0451 f383.9299
linear x-0.4540 y2.9389 f638.0175
linear x0.1564 y1.5451 f816.5357
linear x0.7071 y0.0000 f879.6663
linear x0.9877 y-1.5451 f841.3132
linear x0.8910 y-2.9389 f748.2864
linear x0.4540 y-4.0451 f638.0175
linear x-0.1564 y-4.7553 f504.1828
linear x-0.7071 y-5.0000 f326.0747
linear x-0.9877 y-4.7553 f200.7981
linear x-0.8910 y-4.0451 f383.9299
linear x-0.4540 y-2.9389 f638.0176
linear x0.1564 y-1.5451 f816.5356
linear x0.7071 y0.0000 f879.6663
next

disable x y
exit
```

# Appendix D

# Table of Run Conditions

A listing of typical run parameters used in this experiment. Some of the cases represent several runs taken at different times.

| ramp type | Reynolds number | ramp time (sec) | cylinder diameter (cm) |
|---|---|---|---|
| linear | 1000 | 0.5 | 2.54 |
| -- | -- | 1.0 | -- |
| -- | -- | 2.0 | -- |
| -- | 2000 | 2.0 | -- |
| sin(x) | 1000 | 2.0 | -- |
| 1-cos(x) | -- | 2.0 | -- |

*Table D.1 - Run conditions for starting flow cases.*

| amplitude / diameter | | phase | Reynolds number | period/ Strouhal period | | cylinder diameter (cm) | freestream (cm/sec) |
|---|---|---|---|---|---|---|---|
| streamwise | transverse | | | streamwise | transverse | | |
| n/a | 0.508 | n/a | 1520 | n/a | 1.18 | 2.5 | 6.074 |
| 0.1016 | -- | 0° | -- | 0.569 | 1.14 | -- | -- |
| -- | -- | -45° | -- | -- | -- | -- | -- |
| -- | -- | 180° | -- | -- | -- | -- | -- |
| n/a | 0.508 | n/a | 1090 | n/a | 0.84 | 2.5 | 4.343 |
| 0.1016 | -- | 0° | -- | 0.407 | 0.81 | -- | -- |
| -- | -- | -45° | -- | -- | -- | -- | -- |
| -- | -- | 180° | -- | -- | -- | -- | -- |
| n/a | 0.635 | n/a | 988 | n/a | 1.19 | 2 | 4.94 |
| 0.127 | -- | 0° | -- | 0.578 | 1.16 | -- | -- |
| -- | -- | -45° | -- | -- | -- | -- | -- |
| -- | -- | 180° | -- | -- | -- | -- | -- |

*Table D.2 - Run conditions for oscillating flow cases.*

Fin